

ANALYSIS AND INTERPRETATION OF ALTIMETER SEA ECHO

DONALD E. BARRICK BELINDA J. LIPA

*Ocean Surface Research
Boulder, Colorado*

*Ocean Surface Research
Woodside, California*

1. Introduction	61
2. The Convolutional Representation of the Signal and Its Use	62
2.1. Derivation of Convolutional Form	62
2.2. Recovery of Joint Probability Density from Seasat Data	65
3. Model Fits of Recovered Sea Surface Probability Density	68
4. The Study of Altimetric Biases Using Models	73
4.1. Echo Model with Gaussian Beam/Pulse Shapes and Gram-Charlier Surface Probability Density	73
4.2. Semiempirical Seasat Model, Neglecting Pointing Error	75
4.3. Tracker-Bias Study Using the Semiempirical Model	78
4.4. Antenna Pointing-Error Effects—Model for Echo Plateau	79
4.5. Rain Effects on Altimeter Echo	83
5. Electromagnetic Bias	86
6. A General, Improved Deconvolution Algorithm	93
7. Conclusions	96
Appendix	97
References	99

1. INTRODUCTION

Short-pulse altimetry from space was first suggested in the mid-1960s in a study supported by NASA at Woods Hole, Massachusetts (Ewing, 1965). This study drew on the state of the art of airborne remote sensing as the basis for satellite techniques and applications. Microwave altimeters were proposed for the measurement of sea level, sea state, and tsunamis. Further development of specific sensors for oceanic physics evolved during what has become known as the “Williamstown” study (held at Williams College 5 years after the Woods Hole gathering). Here a strong case was made for microwave satellite altimetry (Kaula, 1970) that provided impetus for the altimeters flown on Skylab and GEOS-3.

In contrast with other microwave instruments (e.g., the scatterometer, radiometer, and synthetic aperture radar), the altimeter is supported by a mathematical model relating the echo to the sea surface interaction that is both noncontroversial and useful for designing algorithms to extract information. Since the backscatter seen by the altimeter in space is restricted to a fraction of a degree around the nadir position, the scattering mechanism is

essentially optics-type reflection from thousands of specular points randomly distributed across the rough, moving sea surface. The mathematical model describing the altimetric echo waveform was derived by Barrick (1972a) using physical optics to represent the scatter from the rough surface. This model is a double integral, and can be written in a convolutional form. It shows that the sea surface response to a short pulse is a ramp starting at zero and rising sharply in time to a plateau, after which it falls off slowly. Sea surface mean position and wave-height information is contained in the ramp portion, called the leading edge. Wind-speed information is extracted from the backscatter signal intensity on the plateau. Models have been devised that are fitted to the leading edge directly to extract mean surface position and wave height, both on board the satellite [for Seasat, see MacArthur (1978) and Townsend (1980)], as well as on earth, post facto (Hayne, 1981).

In this chapter is discussed the physics behind and use of Barrick's model in information extraction and data interpretation. In particular, in Section 2 is presented the convolutional form of the model, demonstrating a much simpler but more illuminating method for its inversion than those used in the above references; it is based on deconvolution by straightforward fast Fourier transform (FFT) algorithms. In the subsequent section the recovered quantity is then interpreted, namely, the sea surface wave-height probability density function in terms of models that allow maximum-likelihood parameter extraction and uncertainty estimation. In Section 4 we develop and employ models to study various factors (both instrumental and near-surface effects) that bias or distort the altimeter echo, and use Seasat to demonstrate their application. In Section 5 we discuss the important and interesting phenomenon called electromagnetic bias, i.e., where the altimeter reckons the mean sea surface position to be, compared with its actual position (with all other errors/biases removed). Finally, in Section 6 a double-deconvolutional-based algorithm for altimeter echo analysis is discussed that can handle various antenna error and rain biases, is computationally efficient, and outputs parameter uncertainties along with the parameters themselves.

2. THE CONVOLUTIONAL REPRESENTATION OF THE SIGNAL AND ITS USE

2.1. Derivation of Convolutional Form

Scatter from a Gaussian, random distribution of rough-surface specular points contained in a downward-propagating spherical altimeter pulse was derived by Barrick (1972a,b) using physical optics, and is repeated here. The result gives the average radar cross section for backscatter, polarized in the

same sense as was transmitted, as a function of time t , while the altimeter receiver is responding to the interaction of its pulse with the rough sea or earth surface. For the coordinate geometry, see Fig. 1.

$$\sigma(t) = 2\pi^2 a^2 |R(0)|^2 \int_0^\infty g(\psi) \sec^4 \theta \sin \phi \left[\int_{-\infty}^\infty P(\xi - \zeta) p_j(\xi) d\xi \right] d\phi \quad (1)$$

where ψ is the angle at the antenna from nadir to a point ζ on the ocean surface; ϕ is the angle at earth center from the satellite to a point ζ on the ocean surface; $g(\psi)$ is the two-way antenna gain pattern, normalized so that it is unity at its maximum (accounts for pointing error); $P(x)$ is the effective pulse shape at the receiver output, normalized to unity at its maximum, versus spatial propagation distance $x = ct/2$; a is the earth's radius; $R(0)$ is the Fresnel reflection coefficient of sea surface at normal incidence; θ is the angle between the local normal to the surface at ζ and the satellite; and $p_j(\zeta)$ is the joint height-slope probability density function of the surface height ζ (positive upward) of the waves above a mean local surface, and wave slopes corresponding to specular angle θ . The above expression is thus far exact; the only approximations implied are those inherent in the specular-point explanation of scatter. For backscatter very near vertical, two decades of experimental data have shown the specular-point model to be totally adequate for the microwave radar echo.

Operation from a satellite such as Seasat requires the use of a narrow-beam antenna, which restricts backscatter to a region very near nadir, i.e., backscatter near the normal or vertical to the mean surface. It is this condition that permits considerable simplification of Eq. (1) to obtain linearization and reduction to a convolutional form. We employ the parameters of Seasat to demonstrate this process. Although exaggerated in Fig. 1, the angles ψ , ϕ , and θ are very small. The angle ψ at Seasat's two-way antenna pattern half-power point is $1.6^\circ/(2\sqrt{2}) \approx 0.57^\circ$. The last sampling gate at which data are taken

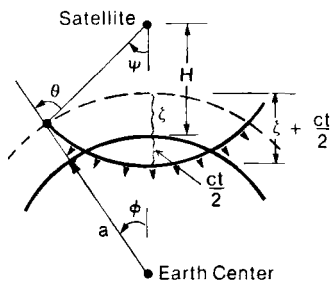


FIG. 1. Coordinate geometry for satellite altimeter; ζ is height of surface point above the mean (spherical) earth/sea, and θ is slope angle (from vertical) seen from altimeter to the mean sea.

and preserved on Seasat (i.e., gate 60) restricts ψ even further; at its altitude of 800 km, ψ at the last gate is 0.3° . Therefore, small-angle trigonometric simplification of the exact law of cosines (see Fig. 1) relating the height ζ of the roughness above the mean spherical earth of radius a to time t and satellite height H , i.e.,

$$(\zeta + a)^2 = (H + ct/2)^2 + (a + H)^2 - 2(H + ct/2)(a + H) \cos \psi \quad (2)$$

yields

$$\zeta = -ct/2 + H'(\psi^2/2) \quad (3)$$

where time t measured at the receiver is taken to be zero when the radar cell center intercepts the mean spherical earth. We also employ the fact that $\zeta \ll H < a$ (for Seasat and the sea, $\langle \zeta^2 \rangle < 5$ m; $H = 800$ km; $a = 6370$ km), and define an "extended" satellite height as $H' \equiv H(1 + H/a)$. We also employ the facts that $\psi = (a/H)\phi$ and $\theta = (a/H'')\phi$, where we define a "reduced" satellite height as $H'' \equiv H/(1 + H/a)$.

In obtaining the final convolutional form for Eq. (1), we change variables of integration from ϕ to $u = a^2\phi^2/2H''$, and replace $ct/2$ by x . The units of the problem are now distance x traversed by the radar cell (measured downward from mean sea level). We also define a normalized radar cross section as $\sigma_s(x) = \sigma(2x/c)/(2\pi^2H''|R(0)|^2)$, and new antenna gain factor as $G(u) = g(\sqrt{2u/H'})$, where $\psi = \sqrt{2u/H'}$. Making these substitutions and simplifications to Eq. (1), we obtain

$$\sigma_s(x) = \int_0^\infty G(u) \left[\int_{-\infty}^\infty P(\xi + x - u) p_j(\xi) d\xi \right] du$$

or

$$\sigma_s(x) = \int_{-\infty}^\infty \int_{-\infty}^\infty p_j(\xi) P(\xi - v) G(v + x) U(v + x) dv d\xi, \quad (4a)$$

where $U(y)$ is the unit step function, defined as

$$U(y) = \begin{cases} 1 & \text{for } y > 0 \\ 0 & \text{for } y < 0 \end{cases}$$

The double-convolutional form of Eq. (4a) is written in concise mathematics as

$$\sigma_s(x) = p_j(-x) \circledast P(-x) \circledast G(-x)U(-x) \quad (4b)$$

where the symbol \circledast denotes convolution. This is precisely the form used by Brown (1977), Walsh (1979), and Hayne (1981). Hayne refers to $G(x)U(x)$ as the "flat-sea impulse response, including antenna pattern and off-nadir effects."

Let us now examine Eq. (4). The altimeter measures $\sigma_s(x)$, on the left side of the equation. $P(x)$ is the pulse shape at the receiver output when the transmitted pulse is sent directly through the receiver; for Seasat, this is measured on board and transmitted to earth, and hence it is known. $G(x)$ is the antenna pattern, and it too is known (when the antenna points toward nadir) from prelaunch calibration measurements. Therefore, all of the desired information about the surface statistics and position is contained in the function $p_j(x)$. We must therefore solve a double, linear integral equation to obtain this function. The measured quantity will have some random noise added to it. This seemingly formidable problem is made quite simple, however, by its convolutional nature. Such convolutional integral equations are most readily solved by Fourier transform procedures. When all of the factors appearing in Eq. (4) are Fourier transformed, the convolutional operator \otimes appearing in Eq. (4b) becomes merely a multiplication sign in the other domain. This procedure is demonstrated in the next section.

2.2. Recovery of Joint Probability Density from Seasat Data

As has been mentioned previously, the usual methods of extracting surface information from altimeter echo data have involved essentially the fitting of a model directly to the echo as a function of time. In this approach, one employs a model for the pulse shape, a model for the antenna gain, and a model for the surface probability density. These are substituted into Eq. (4a) and the integrations are performed to obtain a model for the echo, $\sigma_s(x)$. Since several undetermined parameters appear in the model functions under the integral (e.g., antenna pointing error, tracker error), this integral is usually not soluble in closed form (Hayne, 1981).¹ Then various methods have been used to obtain the best fit possible for the model $\sigma_s(x)$ to the data by varying the parameters of the models under the integral (including least squares, estimates of echo leading-edge slope, etc.)

We are suggesting that a more straightforward and illuminating alternative to these echo/model fits (and less time-consuming numerically) is to solve for the desired functions in Eq. (4) directly by using the unique properties of convolutional integrals and their Fourier transforms. This approach also gives estimates of statistical uncertainties in the derived quantities as an important by-product. Separate models can then be fitted to the recovered functions (if desired), a procedure that is much less time consuming than trying to recover six parameters all at once by the methods mentioned in the preceding paragraph.

¹ In subsequent sections, this integral will be solved in closed form for certain models and assumptions in order to study various biases in altimeter operation.

By restricting attention to the “leading-edge” portion of the echo, Lipa and Barrick (1981) obtained $p_j(x)$ by deconvolution. That method and the results are briefly reviewed here to facilitate understanding of the method and its proposed extension in subsequent sections. The double convolution of Eq. (4) reduces to a single convolution valid on the echo leading edge (where $|x|$ and $|v|$ are small) by differentiating Eq. (4a) with respect to x . Also assumed there is the fact that there is no antenna pointing error, in which case $G(u) \simeq 1$ on the leading edge. Then the expression for the leading-edge derivative or slope is given by

$$\sigma'_s(x) = \int_{-\infty}^{\infty} P(\xi + x)p_j(\xi) d\xi = P(-x) \otimes p_j(-x) \quad (5)$$

Knowing the pulse shape $P(x)$ from samples transmitted to earth during Seasat’s Internal Calibration Mode I, one would theoretically solve this equation for the surface probability density $p_j(x)$ by taking the FFT of $\sigma'_s(x)$, dividing by the FFT of $P(-x)$, and inverse Fourier transforming the quotient back to obtain $p_j(-x)$. Because additive noise is present along with $\sigma_s(x)$, as well as statistical fluctuation in $\sigma_s(x)$ itself (due to the random nature of sea echo), and because the instrument was subject to several observed malfunctions, the procedure was not that simple. Below is a summary of the steps used by Lipa and Barrick in the extraction of $p_j(x)$ ²:

1. Each waveform (every 0.1 sec) is numerically renormalized. This is necessary because the Seasat automatic gain control (AGC) system somehow malfunctions for moderate-to-low sea states, causing approximately every third waveform to be too large (or sometimes too small) by as much as 50%. The renormalization procedure simply divides all gates by the average power level in the last 15 plateau gates (e.g., 45–60).
2. A predetermined number of waveforms are then averaged together. In our case we used both 60 waveforms (over 6 sec or ~ 40 -km groundtrack) and 240 waveforms (over 24 sec or ~ 160 -km groundtrack).
3. The average waveform is broken into its three distinctive regions: pre-leading-edge noise, the leading edge, and the plateau. This is very easily

² Seasat samples the region around $x = t = 0$ as a series of 60 time/range gates 3.125 nsec apart. If the tracker worked perfectly and no other biases were present, $t = 0$ would fall halfway between gates 30 and 31. One hundred power pulses corresponding to $\sigma(t)$ are averaged on the satellite for each gate (each pulse is 1 msec apart) and the 100-sample averages are therefore spaced 0.1 sec apart in time. Three additional “tracking gates” are sampled and transmitted on Seasat; labeled gates 61, 62, and 63, these fall on the leading edge precisely between gates 29 and 30, 30 and 31, 31 and 32. Because of this, these tracking gates are referred to here and elsewhere as gates 29.5, 30.5, and 31.5.

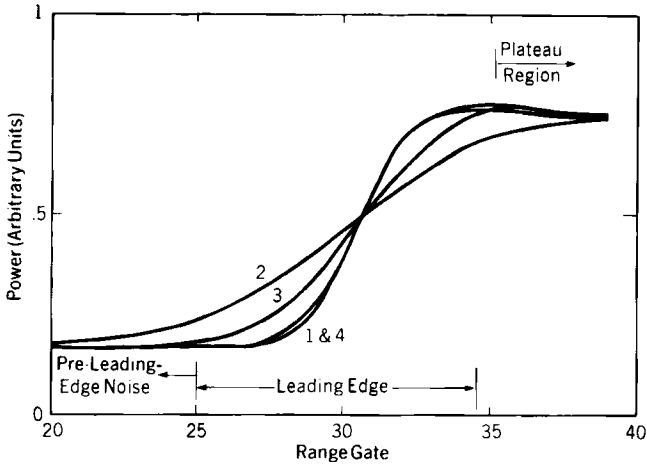


FIG. 2. Leading edges of the returned Seasat altimeter echoes for averages over the samples from orbit 280 shown in Fig. 3. Samples 1 and 4 represent the lowest sea states; sample 2, being closest to the hurricane eye, is the highest.

accomplished by noting changes in slope. (See Fig. 2 for typical, measured altimeter echoes to locate the regions being discussed.)

4. The pre-leading-edge average noise level N_0 is determined and subtracted from the remainder of the waveform. [The pre-leading-edge noise is one of the six parameters determined also by Hayne (1981).]

5. Each waveform gate amplitude is multiplied by an appropriate gain bias correction. For gates 1–60, these were determined and supplied by NASA–Wallops; for tracking gates 61–63, we estimated these corrections ourselves.

6. The derivative of the leading edge, $\sigma'_s(x)$, is then taken using a three-point numerical difference.

7. When deconvolution is used, the FFT of $\sigma'_s(x)$ is taken; the result is then divided by the FFT of the pulse shape, and the inverse FFT is taken again to yield $p_j(\zeta)$, the joint height/zero-slope probability density function. The actual pulse shape determined from the Seasat Internal Calibration Mode I is used rather than a model for the pulse. Because this pulse is so narrow, and therefore measured at a half-gate sampling rate (i.e., every 3.125/2 nsec), and also because the important middle of the leading edge is sampled at this same higher rate, we use a uniform digitization interval of 3.125/2 nsec for the entire leading edge. Hence, waveform regions not sampled at this rate are interpolated to give values at these points. The maximum FFT length required, therefore, to cover the leading edge even in high seas was $N = 64$ points.

8. As a check, and to demonstrate an alternative technique, standard integral inversion was employed on Eq. (5) to give $p_j(\zeta)$. This method also

gives statistical uncertainties in a standard fashion. Theoretically the two techniques give equivalent results. Practically, however, integral inversion (in matrix form) is lengthier timewise, requiring $\sim N^2$ steps compared to $\sim N \log_2(N)$ steps for deconvolution. (This assumes the inverse matrix for the pulse shape $P(x)$ has been obtained and stored as a two-dimensional array earlier.) Time differences between the two methods become significant only for N considerably bigger than 32.

9. Standard covariance techniques (Brandt, 1976) are then used to estimate statistical uncertainties in $p_j(\zeta_i)$ at each height point ζ_i . Here, the covariance matrix of the actual observed echo, $\sigma_s(x_i)$ at consecutive points x_i , is employed rather than theoretical models for these covariances. Lipa and Barrick (1981) found that—for unexplained reasons—the Seasat echo data had a normalized variance that varied with position on the leading edge, and that echo data between consecutive range gates are correlated. Neither of these findings agree with idealized echo theory; therefore, the actual data statistics were used in uncertainty estimates.

Results for four 24-sec samples during a Hurricane Fico overpass (orbit 280; see Fig. 3 for locations) are shown in Fig. 4. Significant wave heights at the four locations are approximately 2.5, 7, 4.4, and 2.6 m. Figure 2 shows the Seasat waveform leading-edge averages for the four times.

In Fig. 4, two curves are shown in each case: one obtained from deconvolution and the other from matrix inversion. In most cases the two curves are so close as to be indistinguishable. This consistency check is one measure of the accuracy of these techniques (no “ground truth” was available beneath the hurricane). Error bars are also shown, representing ± 4 standard deviations. The uncertainties are lower near the wavecrests than toward the wavetroughs, a result of the unexpected variation of normalized echo variance with position on the leading edge.

In the next section we will show how this probability density retrieved from the echo data can be interpreted in terms of ocean surface parameters, both with and without the use of models.

3. MODEL FITS OF RECOVERED SEA SURFACE PROBABILITY DENSITY

As defined after Eq. (1), the probability density function $p_j(\zeta)$ arising from specular-point scattering theory that appears in Eqs. (1) and (4), and that was derived from Seasat data in the preceding section, is a joint sea surface height–slope density. Define $p(\zeta, \zeta_x, \zeta_y)$ as the joint probability density function between the random sea surface wave height $\zeta(x, y)$ and wave slopes $\zeta_x \equiv \partial\zeta(x, y)/\partial x$ and $\zeta_y \equiv \partial\zeta(x, y)/\partial y$, where the x and y lie in the horizontal

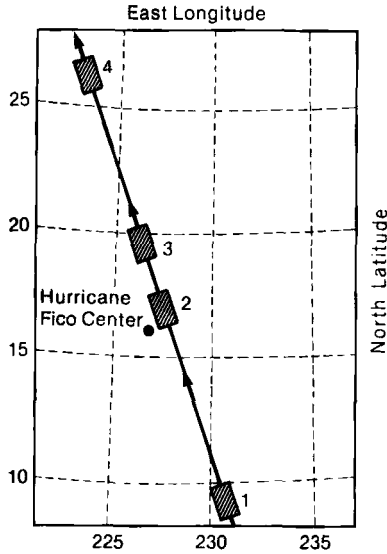


FIG. 3. Location of the four data samples used from Seasat orbit 280, over Hurricane Fico, whose center (the dot) is about 100 km from the altimeter nadir track. Times are as follows: sample 1, 1412:00–1412:24 GMT; sample 2, 1414:42–1415:06 GMT; sample 3, 1415:30–1415:54 GMT; sample 4, 1417:30–1417:54 GMT. Each sample shown is 24 sec long, covering 160 km of ground path.

plane tangent to the spherical earth at the nadir point. Used in relationships for specular-point scatter (Barrick, 1968, 1972a), the slopes in this expression are those required for facets on the waves that can reflect specularly, i.e., whose normals point in the backscatter direction. Since the satellite antenna beamwidth and range gating restrict the slope angle θ [see Fig. 1 and the discussion after Eq. (1)] to be very small, ζ_x and ζ_y are effectively zero in $p(\zeta, \zeta_x, \zeta_y)$ for satellite altimeters; therefore, the axis directions x, y in the horizontal plane are arbitrary. Hence the required expression in Eqs. (1) and (4), and which we derived above, is $p_j(\zeta) = p(\zeta, 0, 0)$.

To lowest order, the sea surface height ζ and slopes ζ_x, ζ_y are zero-mean, Gaussian, uncorrelated random variables. Higher order effects, including correlations between heights and slopes as well as skewnesses (e.g., nonzero wave-height skewness proportional to $\langle \zeta^3 \rangle$, where $\langle \cdots \rangle$ denotes infinite ensemble average) are definitely noticeable, indicating that the sea surface heights and slopes are not *strictly* Gaussian. The non-Gaussian nature of these quantities can be explained by higher order nonlinearities in the hydrodynamic boundary conditions for gravity waves (Longuet-Higgins, 1963). Because of the prospect of extracting additional information about sea state and wave processes from the altimetric echo, it would seem desirable in

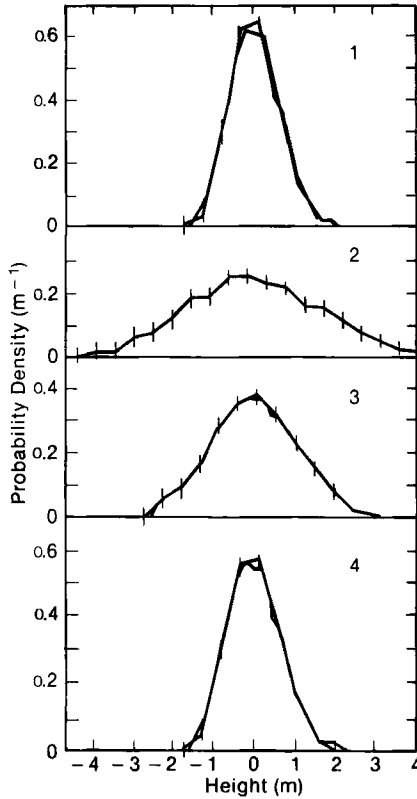


FIG. 4. Surface height-slope probability densities versus surface height for the data samples (1-4) of Figs. 2 and 3, obtained both by matrix inversion and Fourier deconvolution. Averaged over 24 sec, the echo yielded probability density error bars of $\pm 4\sigma$ shown above, for the curve obtained from matrix inversion.

future examination of altimeter algorithms to avoid reducing $p(\zeta, 0, 0)$ to the simple Gaussian height probability (no correlation between height and slopes) with only one parameter (mean-square wave height $h^2 \equiv \langle \zeta^2 \rangle$).

We examine here the fitting of a Gram-Charlier expansion of $p(\zeta, 0, 0)$ to the quantity $p_f(\zeta_i)$ measured in the preceding section. This model takes the following form:

$$\tilde{p}_{jN}(\zeta) = (1/\sqrt{2\pi}h)\{1 + A_1[(\zeta/h)^3] + A_2(\zeta/h)\} \exp(-\zeta^2/2h^2) \quad (6)$$

which contains three unknown parameters, to be determined by fitting Eq. (6) to the functions extracted from Seasat data and shown in Fig. 4. These parameters are h , A_1 , and A_2 . As mentioned above, h is the RMS wave height. $A_1 \equiv \lambda_1/6$, where λ_1 is the height skewness defined as $\lambda_1 \equiv \langle \zeta^3 \rangle/h^3$. For

ocean waves, the fact that this quantity is nonzero and positive is explained by the pointiness near the crests and flatness near the troughs. A_2h includes any shifts of the waveform from its "perfect" location (with gate 30.5 centered halfway up the echo leading edge), normally due to the on-board tracker bias. The quantity A_2h would normally be included in the exponential [i.e., instead of ζ^2 we would have $(\zeta - A_2h)^2$], but since Seasat error A_2h is known to be small in terms of RMS wave height h , this quantity is brought outside by a Taylor series expansion about zero bias, retaining only the first and second terms in A_2h . The resulting model, Eq. (6), is therefore linear in two unknown parameters, A_1 and A_2 , while it is nonlinear only in h . This fact will make least-squares estimation of these three quantities very easy. Finally, we "normalize" the data, $p_{jN}(\zeta_i)$, such that the area under it is unity [i.e., $p_{jN}(\zeta_i) = p_j(\zeta_i)/\sum_i p_j(\zeta_i)$]. We then do a least-squares fit of measured data $p_{jN}(\zeta_i)$ to the model $\tilde{p}_{jN}(\zeta_i)$ by minimizing $\sum_i [p_{jN}(\zeta_i) - \tilde{p}_{jN}(\zeta_i)]^2$ with respect to h , A_1 , and A_2 . Because the model Eq. (6) is linear in A_1 and A_2 , but nonlinear in h , Lipa and Barrick (1981) show that this leads to a simple one-dimensional grid search in h , requiring approximately N^2 steps to find the minimum, with a final interpolation between the three lowest points h_{j-1} , h_j , and h_{j+1} , to give the RMS wave-height estimate \tilde{h} .

There is another obvious way of determining A_2 that does not involve use of a model: direct calculation of the first moment from the retrieved probability density, i.e.,

$$\tilde{\zeta} = \frac{\int_{-\infty}^{\infty} p_{jN}(\zeta)\zeta d\zeta}{\int_{-\infty}^{\infty} p_{jN}(\zeta) d\zeta}$$

This would be identically equal to A_2h if the data fit the model of Eq. (6) perfectly. Theoretically, one can also determine h^2 in this way from the second moment and A_1 or λ_1 from the third moment. There is a problem with higher moments, however. The numerical integration to obtain the moment runs theoretically from $-\infty$ to $+\infty$; practically, one must truncate at some point. Because of noise and statistical fluctuation in the original data, the tails of the retrieved probability $p_{jN}(\zeta)$ never become identically zero, but fluctuate about a low but constant "noise" level. Multiplication of these tails by ζ^n enhances this noise for larger values of n . Therefore, one must truncate the numerical integration at some upper limit to keep this enhanced "tail noise" low. We have found, however, that for larger values of n (e.g., for moments equal to or greater than the second, where $n \geq 2$), the result then becomes quite sensitive to the limit chosen. Hence, our experience with the Seasat data has shown that moments higher than the first cannot be computed stably, and the model-fitting procedure described above must be applied.

In Table I we present values of mean sea-level difference (from gate 30.5) $\tilde{\zeta}$, using both the first-moment and model-fit techniques (along with standard

TABLE I. PARAMETERS OF HEIGHT-SLOPE PROBABILITY DENSITIES FOR SEASAT ORBIT 280

Time (GMT) (hr:min:sec)	Mean sea level difference (cm)		RMS wave height (cm)	Height skewness parameter
	First moment	Model fit		
6-sec averages				
14:12:00-14:12:06	10.4 ± 1	11.0 ± 2	56.3 ± 2	0.22 ± 0.1
14:12:06-14:12:12	10.6 ± 1	11.1 ± 2	59.5 ± 2	0.29 ± 0.1
14:12:12-14:12:18	11.4 ± 1	11.8 ± 2	59.5 ± 2	0.25 ± 0.1
14:12:18-14:12:24	11.4 ± 1	11.9 ± 2	60.5 ± 2	0.30 ± 0.1
14:14:42-14:14:48	35.4 ± 7	51 ± 8	166 ± 5	0.23 ± 0.2
14:14:48-14:14:54	37.4 ± 6	47 ± 9	177 ± 5	0.32 ± 0.2
14:14:54-14:15:00	38.2 ± 6	39 ± 8	169 ± 4	0.08 ± 0.2
14:15:00-14:15:06	35.9 ± 5	36 ± 8	164 ± 4	0.15 ± 0.1
14:15:30-14:15:36	16.4 ± 3	17 ± 5	112 ± 3	0.03 ± 0.2
14:15:36-14:15:42	18.3 ± 3	19 ± 4	110 ± 3	0.13 ± 0.2
14:15:42-14:15:48	14.7 ± 3	16 ± 5	110 ± 3	0.01 ± 0.2
14:15:48-14:15:54	18.2 ± 3	18 ± 4	100 ± 3	0.21 ± 0.2
14:17:30-14:17:36	10.5 ± 2	12 ± 3	65.5 ± 2	0.26 ± 0.1
14:17:36-14:17:42	9.4 ± 2	11 ± 2	64.5 ± 2	0.20 ± 0.1
14:17:42-14:17:48	11.7 ± 2	12 ± 2	64.5 ± 2	0.20 ± 0.1
14:17:48-14:17:54	11.5 ± 2	13 ± 2	62.4 ± 2	0.45 ± 0.1
24-sec averages				
14:12:00-14:12:24	10.8 ± 0.4	11.4 ± 0.5	59.7 ± 0.4	0.27 ± 0.03
14:14:42-14:15:06	41.6 ± 2	47.2 ± 2	167 ± 1	0.27 ± 0.04
14:15:30-14:15:54	17.0 ± 0.7	17.0 ± 1	108 ± 0.8	0.10 ± 0.04
14:17:30-14:17:54	11.1 ± 0.4	11.3 ± 0.6	64.2 ± 0.5	0.29 ± 0.03

deviations or errors in these quantities); positive numbers mean the actual shift from gate 30.5 is upward. The third and fourth columns are RMS wave-height \tilde{h} and height skewness $\tilde{\lambda}_1$, retrieved using the model-fit method. In the top section of this table, each of these is done over 60 total wave forms, comprising 6 sec (~ 40 -km path distance). The bottom section is for a 24-sec average. Table II shows comparisons of RMS wave height \tilde{h} from our method for Hurricane Fico (24-sec averages), compared with the on-board wave-height estimator, as well as algorithms of Fedor and Hayne. (Hayne's data were available for only two of the four periods we analyzed.) These results are taken from Lipa and Barrick (1981).

It is possible to linearize Eq. (6) completely by expanding about an initial estimate of wave height h_0 (obtained either from the on-board wave-height

TABLE II. WAVE-HEIGHT COMPARISONS

Time period	Present analysis (cm)	Fedor (cm)	Hayne (cm)	On board (cm)
14:12:00–14:12:24	59.7	58.8	—	60.5
14:14:42–14:15:06	167	188	128	206
14:15:30–14:15:54	108	117	74	116
14:17:30–14:17:54	64.2	64.7	—	63.7

estimator or from the leading-edge slope). This leads to an iterative search for the true value of h . However, we have found no savings in computer time over the one-dimensional grid search. In addition if h_0 is a poor estimate, the iterative method may converge to an incorrect value. Hence we do not recommend this method.

4. THE STUDY OF ALTIMETRIC BIASES USING MODELS

Thus far, in our convolutional representation for the altimeter echo waveform Eq. (4) we avoided using models for any of the three functions in the integrals that produce the echo: the antenna pattern function, the pulse-shape function, and the surface probability density function. Since the first two should be known from calibration tests of the instruments, the third is obtainable exactly using deconvolution. This method was then tested on Seasat data and the actual probability density was in fact accurately measured. Only in the last section, then, did we fit a model to the surface-height probability density in order to relate its most important descriptors (RMS wave height and wave-height skewness) to the same parameters obtained by other investigators.

There are situations or reasons in which models for all three functions are illuminating. These have to do with how various departures of the system, propagation medium, or scattering process from the ideal affect the echo. Said another way, one can insert biases into the models one at a time and see how the system performs and/or how candidate algorithms will misinterpret the output.

4.1. Echo Model with Gaussian Beam/Pulse Shapes and Gram-Charlier Surface Probability Density

Here we assume a Gaussian shape for the compressed altimeter pulse $P(x)$, with τ being the half-power width of the pulse. Likewise, we assume a Gaussian shape for the antenna beam near its boresight (i.e., the last range gate

taken on Seasat subtends 0.3° from boresight, while the two-way half-power antenna beamwidth extends 0.57° from boresight). At this time we assume the antenna points directly at nadir; pointing-error biases and models will be examined later. The total two-way half-power antenna beamwidth is ψ_H (1.13° for Seasat), from which we define $\psi_b = \psi_H/\sqrt{8 \ln 2}$ and $u_b = H'\psi_b^2/2$. Finally, we define a joint height-slope probability density after the fashion of Eq. (6) that includes height skewness as

$$p_j(\zeta) = p(\zeta, 0, 0) \\ = \frac{1}{(2\pi)^{3/2} h s_x s_y \sqrt{1 - \rho_{xy}^2}} \left\{ 1 + \frac{\lambda_1}{6} \left[\left(\frac{\zeta}{h} \right)^3 - 3 \left(\frac{\zeta}{h} \right) \right] \right\} \exp(-\zeta^2/2h^2) \quad (7)$$

where h is the RMS wave height (related to significant wave height $H_{1/3}$ as $H_{1/3} \simeq 4h$), s_x and s_y are the RMS wave slopes along any two orthogonal axes tangent to the mean sphere, ρ_{xy} is the correlation coefficient of the wave slopes along these axes, and λ_1 is the wave-height skewness coefficient defined after Eq. (6).

Upon substitution of these models into Eq. (4a), the resulting integration can be done in closed form to give

$$\sigma(t) = \sigma(2x/c) = (2\pi)^{3/2} \sigma_o \sigma_\tau H'' \left\{ \frac{1}{2} [1 + \Phi(x/\sqrt{2}\sigma_p)] e^{-x/u_b} \right. \\ \left. + (\lambda_1/12)(\sqrt{2/\pi})(h/\sigma_p)^3 [(x^2/\sigma_p^2) - 1] e^{-x^2/2\sigma_p^2} \right\} \quad (8)$$

where σ_o is the average backscattering cross section per unit area at normal incidence, from which the nadir wind speed is derived (Brown, 1979; Fedor and Brown, 1982); specular-point theory gives the following form:

$$\sigma_o \equiv |R(0)|^2 / (2s_x s_y \sqrt{1 - \rho_{xy}^2}) \quad (9)$$

We also define the following terms

$$\sigma_\tau = c\tau/4\sqrt{2 \ln 2}$$

$$h = \langle \zeta^2 \rangle = \text{RMS wave height}$$

$$\sigma_p = \sqrt{h^2 + \sigma_\tau^2} = (ct_p/2)/\sqrt{2} \quad [t_p \text{ as defined in Barrick (1972a)}]$$

$$u_b = H'\psi_b^2/2 \simeq (ct_s/2)/2 \quad [t_s \text{ as defined in Barrick (1972a)}]$$

and $\Phi(y)$ is the error function of argument y .

Implicit in the above derivation are Seasat altimeter parameters, such that $\tau = 3.074$ nsec (from Seasat internal calibration mode), $t_s = 832$ nsec, $u_b = 3120$ cm. For $h = 0$, $t_p = 1.846$ nsec and $\sigma_p = 19.58$ cm; while for

$h = 200$ cm (i.e., significant wave height is 8 m, representing an extremely high sea state), $t_p = 9.473$ nsec, and $\sigma_p = 201$ cm. Hence, all terms of order σ_p/u_b and higher have been neglected in deriving Eq. (8), since σ_p/u_b is less than 0.03 at even the highest sea states.

The constants in Eq. (8) that determine the model altimeter echo waveform have meaningful physical interpretations. σ_r defines the spatial width of the effective receiver pulse. The quantity $\sigma_p = \sqrt{h^2 + \sigma_r^2}$ defines the amount (in space) to which the pulse is stretched by scattering from the waves of RMS height h ; therefore, this quantity determines the shape of the leading edge. Finally, the quantity u_b , which depends on the antenna beamwidth, is the distance downward the altimeter pulse travels as it expands over the spherical earth until the finite beamwidth attenuates the energy. Hence, t_s and u_H determine the shape of the waveform in the plateau region, as seen from the factor e^{-x/u_b} .

Note at this point that if we take the spatial derivative of Eq. (8) and restrict ourselves to the leading edge (so that $x \ll u_b$), we obtain

$$\sigma'(2x/c) \sim \{1 - (\lambda_1/6)[(x/\sigma_p)^3 - 3(x/\sigma_p)]\} \exp(-x^2/2\sigma_p^2) \quad (10)$$

where if RMS wave height h significantly exceeds pulse width σ_r , we have $\sigma_p \approx h$; therefore Eq. (10) is identical in form to Eq. (7) *except that distance is now turned around* [i.e., wave height in Eq. (7) was upward, whereas x is in the direction of pulse delay time, namely downward]. Therefore, for higher wave heights, the shape of the leading-edge derivative is identically the shape of the Gaussian height density function with the Gram-Charlier correction added to include height skewness. On the other hand, when pulse stretching is small ($h < \sigma_r$) the skewness of wave heights has negligible effect on the altimeter waveform.

The simple, direct relationship between the leading-edge derivative, given by Eq. (10), and wave statistics is attractive, and forms the basis for Fedor's algorithms for extracting wave height (Fedor and Barrick, 1978; Fedor and Brown, 1982).

4.2. Semiempirical Seasat Model, Neglecting Pointing Error

In the preceding section we presented an exact solution for a short-pulse altimeter waveform based on assumed models for the various convolutional factors' constants, as observed in the waveform. Thus system gain, σ_o , and AGC factors are all lumped as one. When this is done, the empirically derived constants truly appear to be independent of sea state, as will be shown subsequently. Therefore, the AGC and height tracker indeed accomplish their functions quite well.

The observed Seasat mean waveform is therefore

$$\sigma_s(2x/c) = N_0 + K \left\{ \frac{1}{2} \left[1 + \Phi \left(\frac{x}{\sqrt{2}\sigma_p} \right) \right] e^{-x/u_b} + \frac{\lambda_1}{12} \frac{2}{\pi} \left(\frac{h}{\sigma_p} \right)^3 \left(\frac{x^2}{\sigma_p^2} - 1 \right) e^{-x^2/2\sigma_p^2} \right\} \quad (11)$$

If the theory that produced the model Eq. (8) that we adapted to Eq. (11) is valid, we should be able to use the nominal constants for σ_p and u_b for Seasat — as measured by the instrument designers and internal calibration mode; this we will do. The remaining constants, N_0 and K , we determine from the analysis of several data sets over the widely varying sea conditions of orbit 280 (the pass over Hurricane Fico analyzed previously). Doing this, we find $N_0 \simeq 5.4$ and $K = 92$, in terms of the units transmitted by the satellite. Because of the AGC and other constants constituting K , we can write $K = A\sigma_o$, where as before, σ_o is the normalized nadir backscattering cross section; A is proportional to (1) AGC gain, (2) a multiplicative factor due to antenna pointing error (to be discussed subsequently), and (3) path attenuation, due in part to rain (to be discussed subsequently). Since the data show that K remains constant, decreases in σ_o for higher winds and seas are compensated by increases in AGC gain A . Therefore, measurement of A gives an uncorrected estimate of σ_o .

The nominal relationship between gate number N ($1 \leq N \leq 60$ for Seasat) and x appearing in Eq. (11) (in the absence of any height biases) is therefore

$$x = x_N = (N - 30.5) \Delta x \quad (12)$$

where $\Delta x = 46.875$ cm based on the sampling time gate $\Delta t = 3.125$ nsec.

To verify the general validity of the empirical model Eq. (11) for the four constants, N_0 , K , σ_p , and u_b (the first two empirically measured and the second two determined from hardware calibration), we plot the model values and measured values in Fig. 5. These two curves represent the lowest and highest sea states in the orbit-280 pass near the hurricane. Significant wave heights for these cases are ~ 2 and ~ 7 m; each sample is an average over 24 sec, consisting of 240 waveforms. The model was plotted using values of \tilde{h} and $\tilde{\lambda}_1$, and bias ζ measured by deconvolution from the data, as described previously and shown at the bottom of Table I. The fit shown in Fig. 5 is reasonably good; the major area of difference between model and data is the plateau, where the actual Seasat echo falls off at a slightly slower rate with time than does the model. The model up to now ignores a number of degradations to both the altimeter return and the system itself. Any or all of these degradations in some combination will cause the measured plateau to droop

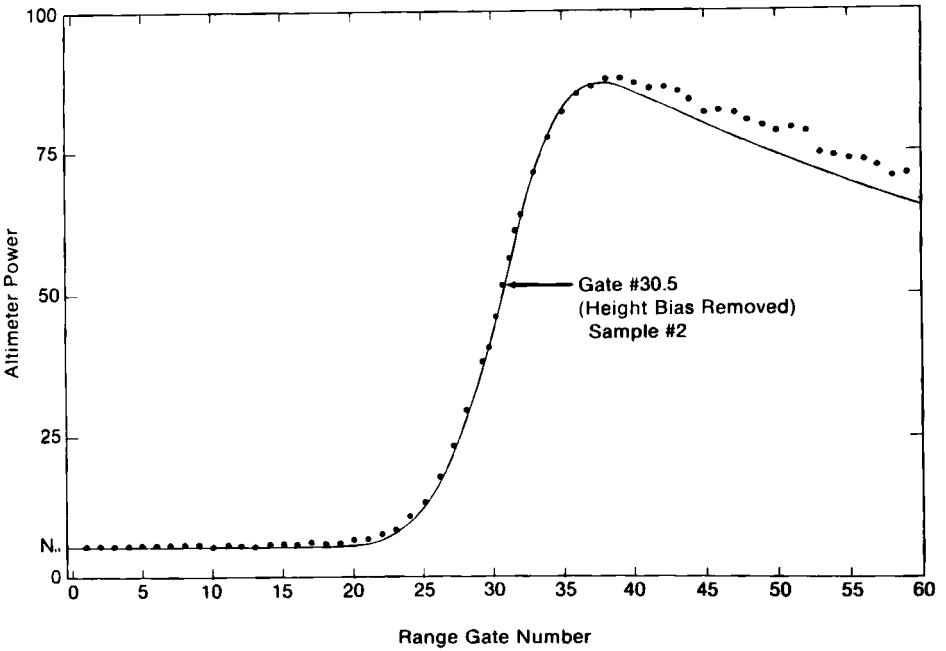
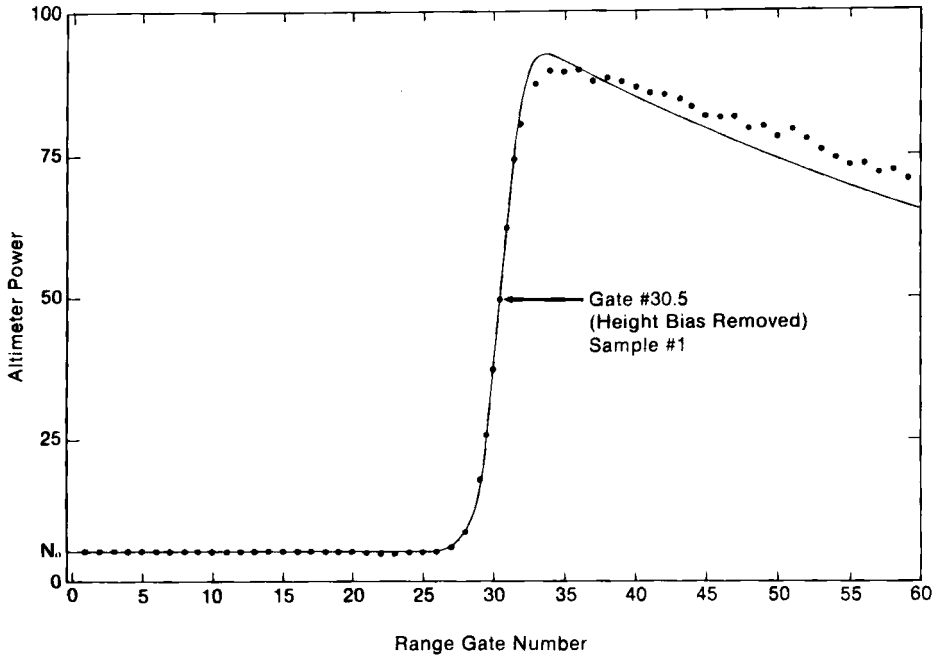


FIG. 5. Data points from Seasat orbit 280 24-sec echo average at sample 1 and sample 2 and fit of model, Eq. (11). Parameter values used in model for h , λ_1 , and height bias are those derived and listed at bottom of Table I, with nominal design values for pulse and beamwidths given for Seasat.

less than the model representing perfect operation. These degradations include the following effects. (1) The actual antenna beamwidth in space could be slightly greater than the nominal value obtained from prelaunch analyses. (2) Very small off-nadir pointing of the antenna boresight will decrease the droop in the plateau. An average pointing error of only 0.3° can explain the observed droop differences, which is not unreasonable to expect. (3) Rain partially filling the altimeter footprint can cause less droop. Both of the latter effects are examined quantitatively in subsequent sections using models for the altimeter return.

4.3. Tracker-Bias Study Using the Semiempirical Model

As mentioned previously, if the Seasat height tracker and AGC circuitry worked perfectly, gate 30.5 would always be centered halfway up the echo waveform leading edge, at the point $t = 0$ and $x = 0$. Therefore, gate 30.5 would itself be an accurate measure of the distance between the satellite and the electromagnetic mean sea surface. Our results (Lipa and Barrick, 1981)—obtained by deconvolution and presented in Table I—show that this is not the case. Others have also found similar differences (Hayne and Hancock, 1982). There is definitely a bias, or difference, between gate 30.5 and the electromagnetic mean surface. Whether deconvolution is employed (as done here), or a model is fitted directly to the actual waveform [as done by Hayne (1981)], the same bias should appear. Either technique, therefore, will be able to measure and remove this bias.

The bias is such that the true electromagnetic mean surface is higher (upward) than gate 30.5. In other words, gate 30.5 is too low, i.e., toward the troughs. Furthermore, this effect is definitely related to sea state, as seen in Table I. It might be suspected that it is also related to wave-height skewness, but since this dependence would be weak, many data sets with accurate independent measurements of skewness would be required to establish this empirically.

To understand this important effect, we have simulated the Seasat tracker/AGC theoretically to study these dependences in greater detail. If our tracker simulation is correct, it should produce results that agree with observations. Such a simulation could then be used (1) to analyze parameter dependences, (2) to establish variations in tracker constants, and (3) for decisions and/or design criteria for future altimeter systems.

The works of MacArthur (1978) and Townsend (1980) detail a simple tracker principle: a feedback system positions gate 30.5 laterally until its amplitude is equal to the *average* amplitude of all 60 waveform gates. Since gate 30.5 corresponds to $x = 0$ in our altimeter model waveform Eq. (11), we

can express this balance condition mathematically as

$$G_0 \sigma_s(-\tilde{\zeta}) = \frac{1}{53} \sum_{i=1}^{60} \sigma_s(\Delta x(i - 30.5) - \tilde{\zeta}) \quad (13)$$

where $\tilde{\zeta}$ represents the difference or error (measured upward) in centimeters from gate 30.5. If the tracker performs perfectly, $\tilde{\zeta}$ will be zero.

The number 1/53 was chosen by MacArthur (1978) and fixed in the hardware rather than 1/60 in the averaging process to account for the expected waveform droop in the plateau region. We have performed independent numerical checks on whether 53 is the optimal number by using our model waveform Eq. (11), and found it indeed to be the closest integer to the true factor.

The factor G_0 accounts for any amplitude bias on gate 30.5. Ideally it should be unity, but we have found from carefully examining many data sets that $G_0 \approx 0.9614$, i.e., gate 30.5 is too high and hence the balance is such that it rides toward the troughs.

The balance condition, Eq. (13), is solved numerically, employing the model Eq. (11) with the nominal Seasat constants given there, and G_0 above; a Newton root finder solves for height bias $\tilde{\zeta}$ as a function of RMS wave height h and wave-height skewness λ_1 . This height-tracker difference $\tilde{\zeta}$ is given in Table III; values in parentheses present $\tilde{\zeta}$ as a percentage of RMS wave height h .

As can be seen, the relation between height bias and wave height is not linear. Rather, the percentage bias increases with both increasing wave height and height skewness. To compare these percentages with observations from Lipa and Barrick (1981), which are repeated in Table I, we employ the same wave-height and skewness parameters as extracted there, and display the results in Table IV.

Table IV shows that observations have a slightly greater bias than do the simulations. The numbers can be made to agree exactly by varying the multiplicative constant G_0 in Eq. (13), to reflect additional unknown gain factors in the circuitry that may have changed after launch. In fact, forcing agreement between simulated and observed values might be used to estimate this gain. Both simulations and observations show greater percentage errors for increasing wave height and skewness. Therefore the general behavior of the simulator algorithm appears correct.

4.4 Antenna Pointing-Error Effects—Model for Echo Plateau

Brown (1977) derived general expressions for the altimeter echo waveform that included the effects of antenna off-nadir pointing errors. We have independently reconfirmed those results. For the Gaussian representation of

TABLE III. SIMULATED VALUES OF MEAN HEIGHT CORRECTION DUE TO TRACKER PERFORMANCE AS A FUNCTION OF RMS WAVE HEIGHT (h) AND WAVE-HEIGHT SKEWNESS (λ_1)

h (cm)	λ_1 (cm)						
	0	0.05	0.10	0.15	0.20	0.25	0.30
0	1.92	1.92	1.92	1.92	1.92	1.92	1.92
25	3.17 (12.7) ^a	3.30 (13.2)	3.44 (13.8)	3.57 (14.3)	3.70 (14.8)	3.83 (15.3)	3.96 (15.8)
50	5.51 (11.0)	5.88 (11.8)	6.26 (12.5)	6.64 (13.3)	7.01 (14.0)	7.38 (14.8)	7.75 (15.5)
75	8.19 (10.9)	8.82 (11.8)	9.44 (12.6)	10.07 (13.4)	10.69 (14.3)	11.30 (15.1)	11.91 (15.9)
100	11.12 (11.1)	12.01 (12.0)	12.89 (12.9)	13.77 (13.8)	14.64 (14.6)	15.50 (15.5)	16.36 (16.4)
125	14.29 (11.4)	15.45 (12.4)	16.60 (13.3)	17.74 (14.2)	18.88 (15.1)	20.01 (16.0)	21.12 (16.9)
150	17.73 (11.8)	19.17 (12.8)	20.60 (13.7)	22.03 (14.7)	23.44 (15.6)	24.84 (16.6)	26.23 (17.5)
175	21.46 (12.3)	23.20 (13.3)	24.93 (14.2)	26.65 (15.2)	28.36 (16.2)	30.04 (17.2)	31.72 (18.1)
200	25.52 (12.8)	27.58 (13.8)	29.63 (14.8)	31.66 (15.8)	33.68 (16.8)	35.67 (17.8)	37.65 (18.8)
225	29.96 (13.3)	32.36 (14.4)	34.74 (15.4)	37.11 (16.5)	39.45 (17.5)	41.77 (18.6)	44.07 (19.6)
250	34.82 (13.9)	37.59 (15.0)	40.33 (16.1)	43.05 (17.2)	45.74 (18.3)	48.41 (19.4)	51.05 (20.4)
275	40.17 (14.6)	43.33 (15.8)	46.46 (16.9)	49.56 (18.0)	52.63 (19.1)	55.66 (20.2)	58.66 (21.3)
300	46.09 (15.4)	49.66 (16.6)	53.21 (17.7)	56.71 (18.9)	60.18 (20.1)	63.61 (21.0)	66.99 (22.3)

^a Values in parentheses are $\tilde{\zeta}$ as a percentage of RMS wave height h .

TABLE IV. COMPARISON OF OBSERVED TRACKER HEIGHT BIASES (AS A PERCENTAGE OF SIGNIFICANT WAVE HEIGHT) WITH THOSE OBTAINED FROM SIMULATIONS USING MODELS AND EQ. (13)^a

Sample no.	RMS wave height (cm)	Observations (%)		Simulations (%)
		First moment	Model fit	
1	59.7	18.1	19.1	15.3
2	167	24.9	28.3	17.5
3	108	15.7	15.7	13.0
4	64.2	17.3	17.6	15.7

^a Nominal Seasat constants were employed in the models, along with retrieved sea surface parameters for the four samples of orbit 280 over Hurricane Fico.

the antenna beam pattern very near boresight, we previously used $G(u) \simeq 1$, which is valid (1) when no pointing error is present, and (2) on the echo leading edge only. A general expression for $G(u)$ that includes angular pointing error β from nadir is obtained by integrating out the azimuthal dependence of the actual antenna pattern around a circular range cell on the surface to obtain

$$U(u)G(u) = e^{-\beta^2/\psi_b^2 - u/\mu_b} I_0[2(\beta/\psi_b)\sqrt{u/\mu_b}] \quad \text{for } u > 0 \quad (14)$$

where $I_0(z)$ is the zero-order modified Bessel function of the first kind with argument z .

Here, we will employ the Gaussian pulse-shape model and Gaussian height probability density (neglecting skewness) in the general echo-waveform double integral, Eq. (4a), to study specifically and separately the effect of pointing error β . Therefore, substituting Eq. (14) into Eq. (4a), along with Gaussian models for the other two functions, and integrating out ξ , we obtain

$$\sigma\left(\frac{2x}{c}\right) = 2\pi H'' \sigma_o \left(\frac{\sigma_\tau}{\sigma_p}\right) e^{-\beta^2/\psi_b^2} \int_0^\infty \exp\left[-\frac{(u-x)^2}{2\sigma_p^2} - \frac{u}{u_b}\right] I_0\left(\frac{2\beta}{\psi_b} \sqrt{\frac{u}{u_b}}\right) du \quad (15)$$

where all of the parameters appearing here have been defined following Eqs. (1) and (8).

Unfortunately, Eq. (15) is not integrable in closed form. Therefore, we have integrated it numerically, normalizing the expression by dividing by $(2\pi)^{3/2} H'' \sigma_o \sigma_\tau$ (such that the plateau becomes unity when $\beta \rightarrow 0$ and $\psi_b \rightarrow \infty$). Results for RMS wave height, $h = 100$ cm, are shown in Fig. 6 for values of antenna pointing error between 0 and 1°, in steps of 0.25°. This is done for the Seasat system, with 60 waveform gates spaced 3.125 nsec (46.875 cm) apart in time (space). In addition, nominal Seasat values for t_s and τ used previously are employed here; a value for τ_b that is larger than Seasat's by $\sqrt{2}$ was used

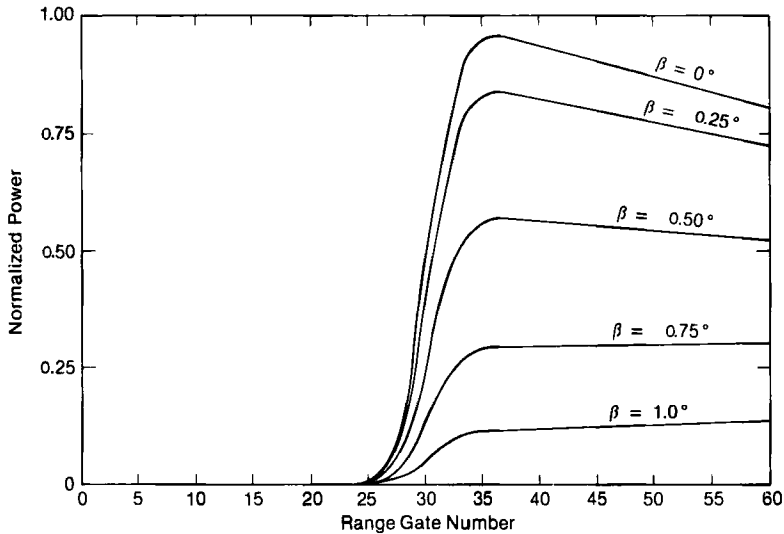


FIG. 6. Model Seasat altimeter echo using Eq. (15), showing effect of antenna pointing error β (in degrees) away from nadir. Nominal Seasat altimeter constants have been used, along with RMS ocean wave height $h = 100$ cm.

for this study. (It is highly unlikely that pointing errors exceeding 1° could occur without track being lost.)

Two effects are evident. As pointing error increases, the overall echo level decreases. This results primarily from the $\exp(-\beta^2/\psi_b^2)$ factor multiplying the integral. The obvious impact of this error will be to give a false value for σ_o as the AGC compensates for this drop. The second effect is the change of the normal plateau "droop" to a "rise." This occurs because of the I_o factor in the integrand, and is explained physically by the fact the largest power level no longer intercepts the earth at nadir (i.e., zero time), but later as the beam points off nadir. Both of these effects, in addition to producing false values of σ_o , will give erroneous mean surface-height values because of combined AGC and height-tracker responses. Fedor has shown that this height error can be several tens of centimeters for a pointing error of only a degree. Therefore, when tilt occurs, it must be identified and taken into account if the parameters obtained from the altimeter are to be meaningful. A simple way to do this follows.

From Fig. 6, it is apparent that—for the 60 waveform gates retained by the Seasat altimeter—the plateau region is very nearly linear. Furthermore, the inclusion of pointing error does not make this region less linear; it merely changes the slope of the plateau. This has led us to derive a very simple, closed-form expression for the plateau. Interpretation of the plateau in terms of this expression can then be used to estimate pointing-angle

error by measuring the slope. Then with the straightforward double FFT deconvolution process discussed subsequently, all pointing errors can be easily and quickly removed.

We define the plateau as the region for which $x > 2\sigma_p$. The integral in Eq. (16) can be solved by the saddle-point method: it is determined by the shape of $\exp[-(u-x)^2/2\sigma_p^2]$ for $u \approx x$. Since x is significantly greater than zero in the plateau, the lower integration limit may be taken to be $-\infty$. Then we do a saddle-point expansion of the exponential argument and integrate, approximating I_0 by its value at the saddle. Then, normalizing by $(2\pi)^{3/2}H''\sigma_o\sigma_r$, we obtain

$$\sigma_n(t) = e^{-\beta^2/\psi_b^2} e^{-2t/t_s} I_0[(2\beta/\psi_b)\sqrt{2t/t_s}] \quad (16)$$

Since the plateau for Seasat has $t \ll t_s$ (e.g., $t = 89$ nsec for the final gate, gate 60, while $t_s \approx 425$ nsec), we can express the exponential in $2t/t_s$ by its first two terms. Furthermore, the modified Bessel function argument is also small in the plateau as long as pointing error β is less than, say, $3\psi_b$; hence it also can be represented by the first two terms of its series expansion. We then obtain the following linear form for the Seasat plateau:

$$\sigma_n(t) = e^{-\beta^2/\psi_b^2} [1 - (2t/t_s)(1 - \beta^2/\psi_b^2)] \quad (17)$$

It can be seen from Eq. (17) that the slope of the plateau increases with β/ψ_b , coming positive when $\beta/\psi_b > 1$. A very straightforward method of measuring pointing error is obvious from Eq. (17). One simply isolates the plateau region (there are always at least 20 gates that define the plateau) and fits a linear regression line to it. The slope of this line is then a direct measure of pointing-angle error β . This method avoids fitting the complicated nonlinear Bessel function convolution to the leading edge (Hayne, 1981).

4.5. Rain Effects on Altimeter Echo

Anomalously high winds obtained from unusually low values of σ_o on the altimeter echo plateau when Seasat passed over storms has led to examination of rain effects on the echo. A uniform rainfall over the entire altimeter footprint (which has a maximum diameter of 10 km corresponding to the last range gate on Seasat) can in principle produce at least three physical effects: (1) attenuation of the signal as it passes through the rain, (2) change in signal phase-path distance due to the slight modification of the refractive index of the rain region, and (3) direct backscatter from the raindrops themselves that fill regions of the altimeter range cells above the sea surface.

The first effect will reduce the absolute level of the entire altimeter echo strength, including the plateau. If ignored, a lower value of σ_o will be deduced, and hence an erroneously high value of wind speed. In Chapter 10 of this

volume, Fedor and Griffith show how this attenuation can be estimated and removed using data from the Seasat Visible and InfraRed Radiometer (VIRR). The second effect—if uncorrected—produces an error in altimeter-derived mean sea level; the VIRR rain estimates are also used subsequently to remove this height bias. When the rainfall is uniform across the cell, however, these two effects do not change the *shape* of the altimeter echo, only its *amplitude* and *time position*. The third effect, namely the rain echo itself, can be shown to be sufficiently small as to be negligible for the short-pulse altimeters flown on Seasat and GEOS; within the cell subtended by Seasat, for example, rain echo is four orders of magnitude lower than sea surface echo, even in a heavy rainfall. Hence, direct raindrop echoes cannot compete with sea echo.³

Examination of rainstorm geometries and their statistics reveals, however, that rain often will not uniformly fill a horizontal cell equivalent to that seen by Seasat (at gate 60, the footprint diameter is ~ 9 km). The more intense the rainfall, the smaller the rain cell on the average (Walsh, 1981). Hence, using models, we examine here the question of whether a typical-size rain cell at an arbitrary location with respect to satellite nadir (either fully or partially filling the altimeter footprint) will produce distortion of the echo because of increased attenuation within the rain region. Referring to Fig. 7, we assume a circularly cylindrical rain cell of height H_c , half-power diameter d , and displacement x_0 from the satellite nadir. Furthermore, for ease of calculation we assume that the rain density—and hence attenuation—falls off in a Gaussian fashion from the cell center at x_0 . Neglecting height skewness here, we then arrive at the following expression for the (normalized) sea surface radar echo as modified by rain attenuation:

$$\begin{aligned} \sigma_N\left(\frac{2x}{c}\right) &= \frac{1}{2} \left[1 + \Phi\left(\frac{x}{\sqrt{2\sigma_p}}\right) \right] e^{-x/u_b} + \frac{1}{\sqrt{2\pi\sigma_p}} \\ &\times A_R e^{-x_0^2/r^2} \int_0^\infty \exp\left[-\frac{(u-x)^2}{2\sigma_p^2} - \frac{u}{u'_b}\right] I_0\left(\frac{2x_0 H \psi_b}{r^2} \sqrt{\frac{u}{u_b}}\right) du \end{aligned} \quad (18)$$

where

$$A_R = 10^{-2k_p H_c/10} - 1$$

$$u'_b = \frac{u_b}{1 + 2u_b H''/r^2}$$

and

$$r = d/2\sqrt{\ln 2}$$

³ Goldhirsh and Walsh (1982) propose a modification to the Seasat design that would purposely measure rain echo above the sea with a future altimeter; however, the rain cell is considerably larger so as to increase the total rain echo.

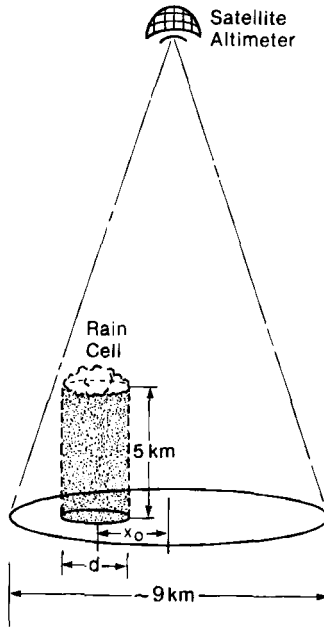


FIG. 7. Geometry for rainstorm model used, which partially fills the Seasat altimeter footprint; the maximum footprint diameter for Seasat is ~ 9 km.

Here, k_p is the one-way signal attenuation rate at 13.5 GHz (in decibels per kilometer) due to rain and H_c is the height of the rain cell. The first term of Eq. (18) is the idealized altimeter sea echo in the absence of rain; the second term therefore represents the correction accounting for rain attenuation.

We employ the above model to calculate numerically altimeter echo curves, assuming an RMS wave height of 100 cm. The echo is plotted as a function of Seasat range gate, with the same altimeter model parameters used for Fig. 6. For the rain, we use the Marshall–Palmer relationship for $k_p = aR^b$ (dB km $^{-1}$), where $a = 2.038 \times 10^{-2}$, $b = 1.023$, and R is rainfall rate in mm hr $^{-1}$ (Goldhirsh and Walsh, 1982). Walsh (1981) employs rainstorm statistics reported by others to establish an inverse relationship between rainfall rate R and storm cell size d ; for example, at $R = 5$ mm hr $^{-1}$ (relatively light rain), the average cell diameter is $d = 36$ km; for $R = 10$ mm hr $^{-1}$, $d = 23$ km; for $R = 20$ mm hr $^{-1}$ (heavy storm), $d = 13$ km. Using these values, we plot normalized altimeter echoes in Fig. 8 with Seasat values for u_b (corresponding to $t_s = 650$ nsec) and H (800 km), with RMS wave height $h = 100$ cm. We take H_c , the effective height of the rain cell column, to be 5 km.

The curves of Fig. 8 show interesting effects and explain some of the strange echo shapes seen by Seasat when it occasionally passed over identified rain

cells. As expected, the severest attenuation and plateau distortion occur when $x_0 = 0$, i.e., when the storm is centered directly beneath the satellite. For light rainfall (Fig. 8a), the attenuation is small; in addition there is almost no distortion (change in slope) to the plateau. The latter is true because with the cell half-power width of 36 km, the 9-km Seasat footprint (out to gate 60) is essentially uniformly filled with rain, no matter where the storm center is located. On the other hand, when rain is heavy (Fig. 8c), plateau distortion is severe when $x_0 = 0$ (i.e., the storm is centered on nadir) because the storm cell width of only 13 km causes an added echo-signal taper across the 10-km footprint. With the rain being severe at nadir, the echo is attenuated greatest on the leading edge, while the echo attenuation becomes less near gate 60 where the annular altimeter cell is out at ~ 9 km.

Even in moderate or light rain, the echo distortion will produce three errors or biases: (1) σ_o on the plateau will be lower, and hence wind speed derived therefrom will be overestimated; and (2) mean sea surface height will be in error by as much as tens of centimeters, depending on how the on-board or post facto algorithms respond to the distorted waveforms. Significant wave height will *not* be appreciably biased by the presence of rain, however.

Although further study and analysis of these and other rain models could be attempted [for example, we could derive a simplified, closed-form expression from Eq. (18) for the line describing the plateau, as we did in Eqs. (16) and (17) for pointing-error effects], such efforts appear rather pointless. This is because the rain models above (and other models) contain too many parameters (unlike pointing error, which has only one parameter). Hence, a confident, unique determination of these parameters and separation from other possible effects (e.g., actual change in σ_o , pointing error) is impossible without additional outside information. Therefore, there is considerable support for both (1) an altimeter modification that would create a special "rain cell" at some distance above the surface to identify rain and parameterize it as much as possible (Goldhirsh and Walsh, 1982); and (2) using other instruments such as infrared and/or microwave radiometers to identify and quantify rain effects (Fedor and Griffith, Chapter 10, this volume).

5. ELECTROMAGNETIC BIAS

Over a decade ago, very short-pulse altimetric measurements of the ocean surface from a tower (Yaplee *et al.*, 1971) uncovered a very interesting phenomenon. When the altimeter beam is so narrow that it essentially profiles the longer waves in height (like a laser), the centroid of the surface echo power is lower in position than the mean sea level as determined by the time-gated echo returns. Said another way, ocean waves are stronger reflectors near their troughs than near their crests. This is not surprising, for the specular-point

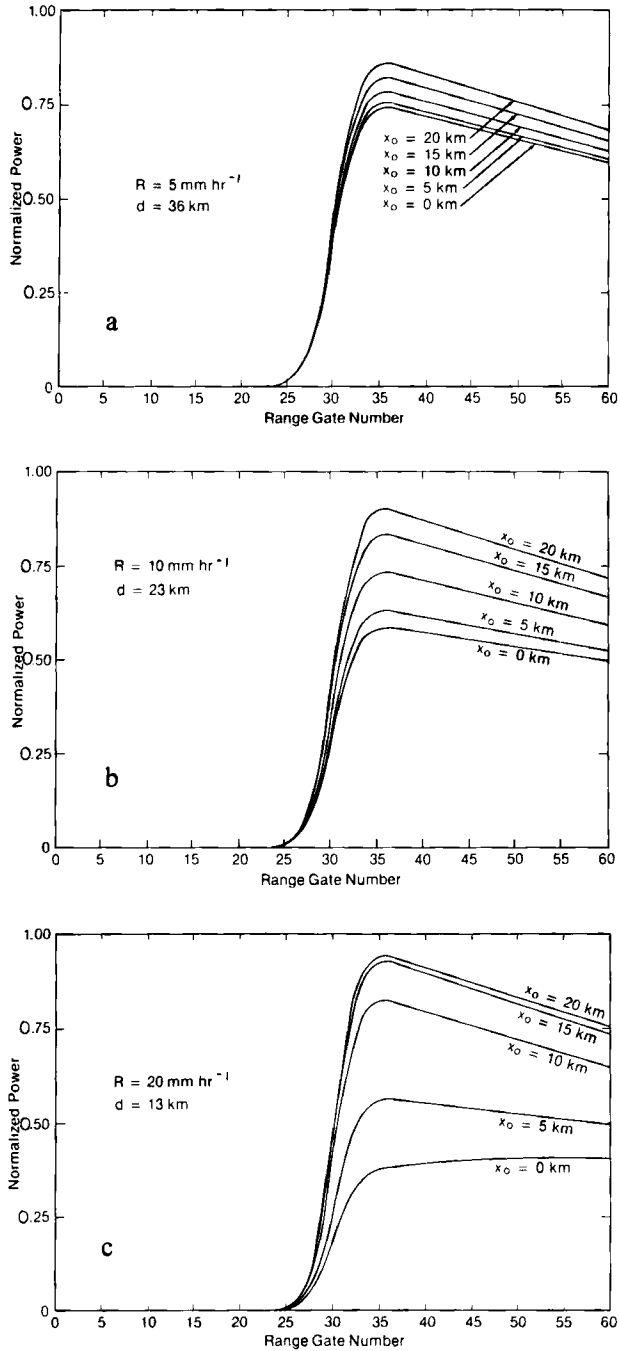


FIG. 8. Model Seasat altimeter echo using Eq. (18), showing effect of rain in distorting the waveform. Here, x_0 is the distance of the rain cell center from nadir, d is the cell diameter [which is related to rainfall rate R by Walsh (1981)]. Nominal Seasat parameter values are used in the model, along with an RMS wave height $h = 100 \text{ cm}$. The three plots represent (a) light, (b) medium, and (c) heavy rainfall.

result for the average backscatter cross section (per unit area) of a rough surface at normal incidence—as given in Eq. (9)—is inversely proportional to surface slopes. Since it is readily observed that ocean waves are pointier at the crests, this inverse relationship between slopes and echo strength confirms that the crest regions should be poorer reflectors than the trough regions. Water waves exhibit this unsymmetrical appearance about the vertical because of the slightly nonlinear hydrodynamic boundary conditions at the air–water interface.

For a typical satellite altimeter (such as Seasat or GEOS), this means that the recovered “mean” sea level extracted from the echo will not coincide with the true mean sea level at that point (the latter defined as the surface within the footprint if all waves came to rest). This altimetric shift downward from the desired, true position has been termed “electromagnetic” (EM) bias. Unlike some of the biases considered in the preceding section, EM bias cannot be easily removed from the apparent height measurement. Although the nonlinear boundary conditions at the sea surface are known exactly, the mathematical methods for solving them have heretofore been too intractable to permit an adequate, quantitative, theoretical investigation of this bias. Therefore, a number of experimental investigations have been undertaken from aircraft over the past years to quantify this effect empirically (Walsh *et al.*, 1983; Choy *et al.*, 1983).

We examine here the theoretical expression—and source—for EM bias in the altimeter echo. Although we have not yet been able to solve the theoretical expression exactly, we obtain bounds for this bias using models in the expression. We interpret these EM bias bounds and compare them with the experimentally observed values cited above.

Longuet-Higgins (1963) showed that a generalization of the Gram–Charlier extension of the Gaussian joint probability density is adequate when the random variables appearing therein are weakly correlated. This generalization can be applied to the joint height–slope probability density function $p_f(\zeta) \equiv p(\zeta, \zeta_x, \zeta_y)$ at $\zeta_x = \zeta_y = 0$, that appears in the altimeter echo of Eqs. (1) and (4), by the simple addition of another term to Eq. (7), giving

$$p(\zeta, 0, 0) = \frac{1}{(2\pi)^{3/2} h s_x s_y \sqrt{1 - \rho_{xy}^2}} \left\{ 1 + \frac{\lambda_1}{6} \left[\left(\frac{\zeta}{h} \right)^3 - 3 \left(\frac{\zeta}{h} \right) \right] - \frac{\lambda_2}{2} \left(\frac{\zeta}{h} \right) \right\} \times \exp(-\zeta^2/2h^2) \quad (19)$$

where for a two-dimensionally rough surface, λ_2 is defined in terms of moments as

$$\lambda_2 = \frac{\mu_{002}\mu_{120} + \mu_{020}\mu_{102} - 2\mu_{011}\mu_{111}}{\mu_{200}^{1/2}(\mu_{020}\mu_{002} - \mu_{011}^2)} \quad (20)$$

with the moments μ_{lmn} defined as $\mu_{lmn} = \langle \zeta^l \zeta_x^m \zeta_y^n \rangle$.

For example, the second moments take the following familiar forms:

$$\begin{aligned}\mu_{200} &= \langle \zeta^2 \rangle = h^2 & \mu_{020} &= \langle \zeta_x^2 \rangle = s_x^2 \\ \mu_{002} &= \langle \zeta_y^2 \rangle = s_y^2 & \mu_{011} &= \langle \zeta_x \zeta_y \rangle = s_x s_y \rho_{xy}\end{aligned}$$

where we have taken our local coordinate system such that all first moments are zero, i.e.,

$$\mu_{100} = \langle \zeta \rangle = 0 \quad \mu_{010} = \langle \zeta_x \rangle = 0 \quad \mu_{001} = \langle \zeta_y \rangle = 0$$

If we restrict ourselves to a one-dimensional (collinear) sea with waves propagating in the x direction, the expression Eq. (19) for the Gram-Charlier model is modified by changing the constant before the braces to $1/2\pi h s_x$, and we have $\lambda_2 = \mu_{120}/(\mu_{200}^{1/2}\mu_{020}) = \langle \zeta \zeta_x^2 \rangle / (h s_x^2)$, a result derived by Longuet-Higgins (1963) and Jackson (1979). We see in this much simpler, collinear form for λ_2 that it is directly proportional to $\langle \zeta \zeta_x^2 \rangle$, the correlation between height and the square of the slope. This quantity is obviously nonzero and positive for a surface like the sea that is pointier near the crests ($\zeta > 0$), where the mean-square slopes will be greater.

Therefore, the term $-(\lambda_2/2)(\zeta/h)$ appearing in Eq. (19) represents a bias downward by an amount

$$\zeta_{EM} = -(\lambda_2/2)h = -(\lambda_2/8)H_{1/3} \quad (21)$$

in terms of RMS or significant wave height. It has been observed in many of the previously cited experimental investigations that EM bias is definitely proportional to wave height, and those investigators present their results as a percentage of significant wave height $H_{1/3}$.

To pursue the theoretical expressions and their interpretation a bit further, we employ perturbation theory to find expressions for the third moments required in λ_2 , as done in Longuet-Higgins (1963), Weber and Barrick (1977), and Barrick and Weber (1977):

$$\mu_{300} \equiv \langle \zeta^3 \rangle = 3 \iint d^2 \bar{k}_1 \iint d^2 \bar{k}_2 S(\bar{k}_1) S(\bar{k}_2) \sum_{m=\pm 1} A(\bar{k}_1, \sqrt{gk_1}, m\bar{k}_2, m\sqrt{gk_2}) \quad (22a)$$

$$\begin{aligned}\mu_{120} = \langle \zeta \zeta_x^2 \rangle &= \iint d^2 \bar{k}_1 \iint d^2 \bar{k}_2 S(\bar{k}_1) S(\bar{k}_2) \sum_{m=\pm 1} [(k_{1x} + mk_{2x})^2 - mk_{1x}k_{2x}] \\ &\times A(\bar{k}_1, \sqrt{gk_1}, m\bar{k}_2, m\sqrt{gk_2})\end{aligned} \quad (22b)$$

$$\begin{aligned} \mu_{102} \equiv \langle \zeta \zeta_y^2 \rangle &= \iint d^2 \bar{k}_1 \iint d^2 \bar{k}_2 S(\bar{k}_1) S(\bar{k}_2) \sum_{m=\pm 1} [(k_{1y} + mk_{2y})^2 - mk_{1y} k_{2y}] \\ &\times A(\bar{k}_1, \sqrt{gk_1}, m\bar{k}_2, m\sqrt{gk_2}) \end{aligned} \quad (22c)$$

$$\begin{aligned} 2\mu_{111} \equiv 2\langle \zeta \zeta_x \zeta_y \rangle &= \iint d^2 \bar{k}_1 \iint d^2 \bar{k}_2 S(\bar{k}_1) S(\bar{k}_2) \\ &\times \sum_{m=\pm 1} [(k_{1x} + mk_{2x})(k_{1y} + mk_{2y}) \\ &+ (k_{1x} k_{1y} + k_{2x} k_{2y})] A(\bar{k}_1, \sqrt{gk_1}, m\bar{k}_2, m\sqrt{gk_2}) \end{aligned} \quad (22d)$$

where $S(\bar{k}_i)$ is the wave-height directional spectrum at wavenumber $\bar{k}_i = k_{ix}\hat{x} + k_{iy}\hat{y}$. The "coupling coefficient" A is obtained from the perturbational solution to the nonlinear surface boundary conditions for gravity waves, and correcting a factor of 2 in the Longuet-Higgins (1963) and Jackson (1979) expressions, is given by Weber and Barrick (1977):

$$A(\bar{k}_1, \omega_1, \bar{k}_2, \omega_2) = \frac{1}{2} \left[k_1 + k_2 + \frac{k_1 k_2 - \bar{k}_1 \cdot \bar{k}_2}{\omega_1 \omega_2 / g} \left(\frac{gK + \Omega^2}{gK - \Omega^2} \right) \right] \quad (23)$$

where

$$\bar{K} \equiv \bar{k}_1 + \bar{k}_2 \quad \Omega \equiv \omega_1 + \omega_2 \quad k_1 \equiv |\bar{k}_1| \quad k_2 \equiv |\bar{k}_2| \quad K \equiv |\bar{K}| \quad (24)$$

and g is the acceleration of gravity.

Second moments needed are easier:

$$\mu_{200} = \langle \zeta^2 \rangle \equiv h^2 = \iint d^2 \bar{k} S(\bar{k}) \quad (25a)$$

$$\mu_{020} = \langle \zeta_x^2 \rangle \equiv s_x^2 = \iint d^2 \bar{k} S(\bar{k}) k_x^2 \quad (25b)$$

$$\mu_{002} = \langle \zeta_y^2 \rangle \equiv s_y^2 = \iint d^2 \bar{k} S(\bar{k}) k_y^2 \quad (25c)$$

$$\mu_{011} = \langle \zeta_x \zeta_y \rangle \equiv s_x s_y \rho_{xy} = \iint d^2 \bar{k} S(\bar{k}) k_x k_y \quad (25d)$$

As long as one is willing to specify the form of a model for the wave-height directional spectrum $S(\bar{k})$, the preceding expressions show that in principle the integrals of Eqs. (22) and (25) should be solvable at least numerically and

should produce results for EM bias, as represented by λ_2 . Obviously the factor λ_2 depends in a very complicated way on the nature of the directional spectrum and its parameters, and hence EM bias would be expected to be a function of more variables than merely significant wave height.

Jackson (1979) solved for λ_1 and λ_2 in closed form for the simpler case of collinear wave fields ($\zeta_y \equiv 0$), but obtained values for EM bias that were considerably larger than those observed experimentally. This is now known to be due to the breakdown of the perturbation theory basis for Eq. (22) at large wavenumbers, k_1 and k_2 . This breakdown manifests itself in the fact that A given in Eq. (23) "saturates," i.e., no longer continues to increase in proportion to k_1 and/or k_2 beyond a certain point. This saturation effect is only important in Eqs. (22b)–(22d) because the overall integral is quite sensitive to short waves, i.e., large k_1 and k_2 . It would be ideal to have an expression for A that accounts for this "saturation effect" but such an expression has not yet been calculated.

The point at which perturbation theory breaks down and A saturates occurs when the perturbational parameters $k_1 h$ and $k_2 h$ are near unity. Since A no longer increases beyond that point, an approximation that can give bounds to EM bias is obtained here by truncating the integrals in Eqs. (22b)–(22d) at upper limits defined by k_{1u} , $k_{2u} = f/h$, where f is near unity. We employ a JONSWAP (Joint North Sea Wave Project) model for the wave spectrum $S(\bar{k})$ (Hasselmann *et al.*, 1973, 1976, 1980), which is presently believed to provide the best parametric representation of waves versus wind, fetch, and duration; empirically "tuned," this model incorporates features predicted by nonlinear wave-wave energy transfer. It is adapted from the above references and transformed to wavenumber variables in the appendix to this chapter.

Whereas the third moments defined in Eqs. (22b)–(22d) have their upper limits defined as described above to approximate the saturation effect, the integrals for the second moments defined in Eq. (25) are truncated in another way. Again, only Eqs. (25b)–(25d) are sensitive to the choice for the upper limit because the appearance of wavenumber squared in the integrand enhances the effect of the smaller scale roughness (at larger wavenumbers) in contributing to the slopes. Truncation at some point is necessary, for if we assume the usual equilibrium-range spectral behavior (i.e., f^{-5} frequency dependence) used in Phillips, Pierson–Moskowitz, and JONSWAP models, these slope integrals diverge as the upper limit goes to infinity. On physical grounds, therefore, we take the upper limit to be $k_u \simeq k_0/20$, where k_0 is the radar wavenumber. For sea surface gravity waves, it is approximately at this point beyond which (in wavenumber) specular points no longer contribute to the scattering process. For the f^{-5} equilibrium-range wave spectral behavior, however, this exact upper-limit value is not that critical; for example, the use of $k_0/10$ would have produced a change in the second-moment (mean-square slope) integrals of

$\sim 14\%$, or 0.5 dB. We therefore will employ $k_u = k_0/20 \simeq 30 \text{ m}^{-1}$ as an upper limit in ensuing examples, corresponding to the Seasat altimeter operating frequency of 13.9 GHz.

Using the JONSWAP wind-wave spectral model adapted in the appendix to this chapter and the upper limits defined for Eqs. (22) and (25), we numerically evaluate these integrals, understanding that they are only approximations. (More exact evaluations await the derivation of a correct theory explaining saturation.) If we evaluate λ_2 defined in Eq. (20), then EM bias given by Eq. (21) in terms of λ_2 bears an explicit direct proportionality to RMS or significant wave height. We find, however, that λ_2 evaluated in the above approximate manner still retains a weak, inverse power-law dependence on significant wave height, independent of the JONSWAP spectral development parameter ν (the latter is taken to be ~ 0.14 for fully developed seas, increasing to possibly 0.3 for newly arising or fetch-limited seas). A regression, power-law fit to the numerical results for $f = 1$ gives

$$\lambda_2 \simeq 0.25H_{1/3}^{-0.28} \quad (26)$$

Individual scatter in the theoretical model results for λ_2 from the above best-fit model does not exceed ± 0.06 when significant wave height is greater than 0.2 m. A change of $\pm 50\%$ in the upper integration limit on third moments—as represented by the factor f —results in corresponding changes of $\pm 20\%$ in λ_2 .

Recent experimental determinations of EM bias have been undertaken using a contouring radar from an aircraft at 36 GHz (Walsh *et al.*, 1983), and using a microwave altimeter from an aircraft at 10 GHz (Choy *et al.*, 1983). Walsh's results at the higher frequency show an EM bias of -1.1% of significant wave height, with a scatter between -0.5 and -2.0% ; no obvious trend of EM bias (expressed as a percentage of significant wave height) versus significant wave height is seen from Walsh's data. Choy, on the other hand, finds an EM bias of -3.5% of significant wave height at the lower radar frequency, with a scatter between -2.0 and -5.0% . The significant difference versus radar frequency is surprising and as yet unexplained quantitatively. Using the crudely estimated theoretical expression for λ_2 of Eq. (26) in Eq. (21), we find at 13.9 GHz that EM bias varies between -3.0 and -2.0% for significant wave heights between 1.0 and 5.0 m, respectively. With $\pm 20\%$ uncertainty (at least) because of the upper-limit approximation, our values fall between those of Walsh and Choy. The scatter in the measurements, as well as the approximations employed in the theoretical predictions, preclude serious attempts at more detailed quantitative comparisons.

The reason for the considerable experimental investigations of EM bias—and also more exact theoretical studies—is to understand this effect by noting

which surface parameters (in addition to significant wave height) cause variation in λ_2 . The above experimental studies attempt to correlate EM bias to such things as surface wind speed, wave-height skewness, dominant wave period, and wave-height kurtosis. The correlations obtained by the two investigators appear in some cases to be at odds with each other. The number of data points employed in the analyses is too meager to pinpoint the source of these correlation differences. Needless to say, additional studies (both theoretical and experimental) will be required to quantize the dependences of EM bias more accurately.

In summary, both the experimental and theoretical results show that—at Seasat operating frequencies—EM bias can be -15 cm at 5 m significant wave height, with actual variations about this mean value between -10 and -25 cm (at the same wave height). Such a bias, and particularly its uncertainty, lies well beyond the desired accuracy limits for satellite altimetric sea surface height measurement applications. The present inability to remove it from the data (in contrast, for example, with tracker bias) further encourages attempts to correlate EM bias to other sea surface parameters that can be measured by independent satellite techniques, so that this source of considerable error can be eliminated and/or reduced.

6. A GENERAL, IMPROVED DECONVOLUTION ALGORITHM

Lipa and Barrick (1981) developed and demonstrated a simple, efficient algorithm that can be applied to the echo leading edge involving a single deconvolution; we summarized that investigation previously. That method will not work for the plateau region, however. More important, when antenna pointing-error effects are present, that method will fail for both the plateau *and* leading edge. Therefore, we introduce here a general double-deconvolutional algorithm that can be used when pointing error contaminates the echo.

The algorithm proposed is efficient, in that it does not attempt to determine six parameters all at once from a least-squares model fit to the entire echo waveform. It identifies and analyzes separately the three easily recognizable portions of the sea echo: (1) the pre-leading-edge noise level N_0 , (2) the leading edge, and (3) the plateau. From the plateau, we do a linear regression fit based on Eq. (17) to determine the pointing error β , if any. Then we know two of the three quantities occurring in the double convolution on the right side of Eq. (4): (1) the pulse shape $P(u)$, obtained from the internal calibration mode, and (2) the antenna gain factor $G(u)U(u)$, with $G(u)$ given by Eq. (14) when pointing error is present. The unknown but desired quantity is the third factor in the double convolution: the surface height–slope probability density $p_f(\zeta)$.

The latter is obtained by divisions of the Fourier transforms of known quantities. Define

$$F(P(u)) \equiv Q(\eta) = \int_{-\infty}^{\infty} P(u)e^{-i\eta u} du \quad (27)$$

with

$$F(\sigma_s(x)) \equiv S_s(\eta) \quad F(p_j(\zeta)) \equiv q_j(\eta) \quad F(G(u)U(u)) \equiv H(\eta) \quad (28)$$

being Fourier transforms of the other quantities defined similarly. Then, because of Eq. (4), the Fourier transform of the desired quantity, $q_j(\eta)$, is given by

$$q_j(\eta) = S_s(-\eta)/Q(\eta)H(\eta) \quad (29)$$

Then the desired quantity is obtained by an inverse FFT, i.e.,

$$p_j(\zeta) = F^{-1}(q_j(\eta)) = (1/2\pi) \int_{-\infty}^{\infty} q_j(\eta)e^{i\zeta\eta} d\eta \quad (30)$$

It is important to note that it is necessary to actually do FFTs only twice: once on $\sigma_s(x)$ and once again on $q_j(\eta)$. The Fourier transform of $P(u)$, namely $Q(\eta)$, is done once for the pulse obtained from the calibrate mode and stored as a table. (The pulse shape does not appear to change over many orbits.)

The Fourier transform of the antenna gain factor is known in closed form. Substituting Eq. (14) into Eq. (27), we find from integral tables that

$$H(\eta) = \frac{u_b}{1 + i\eta u_b} \exp \left\{ \frac{-i\eta u_b \beta^2 / \psi_b^2}{1 + i\eta u_b} \right\} \quad (31)$$

As a check on Eq. (31), note that as $u_b \rightarrow \infty$ (i.e., the antenna becomes omnidirectional in its gain pattern), we obtain $H(\eta) \rightarrow 1/i\eta$, which is the Fourier transform for the unit step function. This is as it should be, as one sees from Eq. (14), where the unit step is all that is left in this limit. In other words, if the beamwidth is large enough, pointing error obviously does not matter.

Therefore, a general, double-deconvolutional algorithm incorporating these effects and producing real-time uncertainties in desired output parameters is summarized here, based on the Seasat altimeter:

1. Renormalize each waveform (every 0.1 sec) to correct occasional high and low waveforms caused by AGC malfunction. This is done by dividing each waveform by the average energy in gates 45–60.

2. Average a desired, predetermined number of waveforms together.

3. Multiply all range-gate amplitudes by predetermined gain bias corrections.

4. Identify and separate the three characteristic portions of the waveform: pre-leading-edge noise, the leading edge, and the plateau. Store the gate positions representing the beginnings and ends of these three segments. This separation is easily done by noting the maximum slope for the three middle gates, and using a simple predetermined criterion for these gate positions based on this slope.

5. Fit a straight, horizontal line to the pre-leading-edge portion. Determine the mean and standard deviation of this constant.

6. Subtract the constant determined in (5) from each gate amplitude constituting the remaining two waveform regions.

7. Fit a linear regression line to the plateau segment. Determine from Eq. (17) the amplitude constant for the plateau, the pointing-angle error β from the slope, and the standard deviations in these quantities.

8. Use the constant and β to do a first correction to the σ_o value obtained from the AGC gain. Rain corrections, if applicable and desired, can then be applied to σ_o .

9. Deconvolve the leading-edge waveform segment using Eqs. (27)–(31) to obtain the joint height–slope probability density for the sea. Lookup tables of the Fourier transform of the pulse (obtained from the internal calibration mode) are divided into the Fourier transform of the leading edge. Likewise, the Fourier transform of the antenna beam factor including the tilt β is simply calculated from Eq. (31) and divided into the leading-edge Fourier transform also. Then the inverse FFT of this quantity [i.e., Eq. (30)] gives the desired probability density.

10. Renormalize the probability density so that the area under it is unity; this is simply done by dividing the probability density at each gate position by the sum over all gate positions.

11. Using matrix covariance techniques employed in Lipa and Barrick (1981), determine uncertainties in the probability density at each gate position.

12. Fit the three-parameter model of Eq. (6) (linear in two parameters: height skewness and height bias) to the recovered probability density. Do a one-dimensional grid search to determine wave height. These techniques are tested and described in Section 3.

13. Use linear error propagation theory and covariance matrix methods (as done in Lipa and Barrick, 1981) to determine the statistical uncertainties in waveheight, skewness, and height bias.

14. Determine nadir wind speed from σ_o using the best, empirically supported model function available at the time.

This method has the following advantages over versions that attempt to fit a model with six parameters to the entire leading edge by least-squares methods (Hayne, 1981):

1. It provides the complete joint height probability density function for the sea surface, rather than a two-parameter description of it. This additional information will prove useful for future research and applications involving ocean surface processes. If the same two parameters are desired, they have been shown in Lipa and Barrick (1981) to be easily obtainable from this probability density function.

2. Because of the natural segmentation of the waveform into its three constituent regions, our method is much more efficient in terms of computer operations and time.

3. The method here, not involving multiparameter grid searches and/or matrix inversions, is stable. If one attempts to get around a time-consuming, multidimensional grid search, the usual procedures are (a) to linearize the model about initial guesses for the several parameters and then solve the least-squares problem by matrix inversion; (b) to "home in" on the minimum in an iterative fashion, starting with an initial guess and using a variation of a root-finding scheme. One hopes these will converge to the solution. When noise is present, however, a poor initial guess can cause either no convergence, or worse yet, convergence to parameters that represent the least-squares solution for a *local* minimum rather than the *global* minimum. The present algorithm involves no initial guess or repeated iterations, and hence cannot be unstable.

4. The present approach uses standard matrix covariance and linear error propagation techniques to output statistical uncertainties (or confidence limits) for all derived quantities continuously; no other existing algorithm does this.

7. CONCLUSIONS

Much is known about the interaction of the altimeter pulse with the ocean surface. Solutions based on specular-point scatter theory show that the echo waveform is a double convolution. This special form of a double-integral equation has been inverted—or deconvolved—using FFT methods, yielding the surface wave-height and slope probability density in a very efficient algorithm. A straightforward least-squares model fit to this probability density (nonlinear in only one parameter) then yields wave height, mean surface position, and wave-height skewness. Uncertainties in these three parameters are routinely provided by the algorithm. Tested with Seasat data for a pass over Hurricane Fico (orbit 280), these uncertainties for a 160-km section of path data are 0.7, 4, and 15% (RMS) of the mean values, respectively.

Models for the sea surface probability density are used to study and interpret other biases quantitatively. For example, the Seasat height tracker

outputs a mean height position that is biased downward by an amount between 3.5 and 6.5% of significant wave height. This bias is sea-state dependent, but can be removed by an algorithm that fits a model to the inverted echo waveform.

Both antenna beam pointing error and moderate rain within the radar cell can distort the echo severely, and if uncorrected will produce values for height and wind speed (deduced from the plateau backscatter cross section, σ_o) that are grossly in error. Pointing error is easily removed when it occurs by a double-deconvolutional algorithm described here; its magnitude is first measured by either (1) using an independent attitude sensor or (2) measuring the slope of the echo plateau. Rain distortion is not easily removed. The best hope appears to be to identify those situations when rain is present (either from independent measurements or from the distorted altimeter signal itself) and throw out those samples whose distortion exceeds a certain amount.

Electromagnetic bias is a height error not easily removed. Although it varies with sea state, it is seen to depend significantly on other factors also. Quantitative estimates of these dependences from both theoretical and experimental investigations are as yet incomplete. Since altimeter-measured surface heights can be in error by as much as 15–25 cm because of EM bias, further investigations are necessary if accurate sea surface topography is to be realized from future altimeters.

We present a brief outline of an efficient, alternative algorithm for the altimeter echo, different from those presently being employed. It incorporates most of the techniques studied in this manuscript for interpreting biases and the echo waveform statistics. Furthermore, it can provide uncertainties in all of the extracted parameters—along with the parameters—so that the user can decide how or whether to apply each geophysical data record.

APPENDIX

A definitive series of experiments done over a decade ago resulted in the synthesis of a new model—called the JONSWAP spectrum—for the wave-height directional spectrum that supports the theoretical concepts of non-linear energy transfer to the longer ocean waves developed by Hasselmann in the early 1960s. The first studies (Hasselmann *et al.*, 1973, 1976) developed a parametric representation for the nondirectional temporal wave-height spectrum. The term “parametric” refers to the fact that this spectrum has the same shape regardless of the physical conditions producing it. For the user, only two parameters are needed to produce the final, absolute spectrum: the wind velocity $\bar{u} = (u, \theta_w)$ and the development factor v . The latter is shown experimentally to be a function of fetch (i.e., the distance over which the wind

has blown at a more or less constant velocity), and is known to depend on the duration (i.e., the time during which the wind has blown at a constant velocity). For "fully developed" seas (where the fetch and duration are very large), $v \simeq 0.14$, whereas it increases to 0.25–0.4 for seas that are less than fully developed.

Recently the nondirectional spectrum has been extended (Hasselmann *et al.*, 1980), based on the same measurements, to include a directional factor, resulting in a complete model for the wave-height directional spectrum. The directional factor is parametric also, being a function of the same two parameters as the nondirectional factor. The spectrum peaks azimuthally, of course, along the wind direction θ_w ; it is narrowest in angular spread at frequencies or wavenumbers near the most energetic waves, and tends to isotropic in angle toward the shorter waves.

Here, we put both the nondirectional and directional factors together, and convert to wavenumber k [$\bar{k} = (k, \theta)$] rather than wave frequency f . The resulting model is then defined as

$$S_j(\bar{k}) = S_j(k, \theta) \equiv f(k)g(k, \theta) \quad (\text{A1})$$

normalized such that

$$h^2 = \mu_{200} = \int_0^\infty k dk \int_{-\pi}^\pi d\theta S_j(k, \theta) = \int_0^\infty f(k)k dk \quad (\text{A2})$$

where

$$\int_{-\pi}^\pi g(k, \theta) d\theta = 1 \quad (\text{A3})$$

The nondirectional spectral factor is given by

$$f(k) = \frac{\alpha}{2k^4} \exp \left\{ -\frac{5}{4} \left(\frac{k_m}{k} \right)^2 + (\ln \gamma) \exp \left[-\frac{(\sqrt{k} - \sqrt{k_m})^2}{2\sigma^2 k_m} \right] \right\} \quad (\text{A4})$$

where

$$\sigma = \begin{cases} \sigma_a = 0.07 & \text{for } k \leq k_m \\ \sigma_b = 0.09 & \text{for } k \geq k_m \end{cases}$$

$$\gamma = 3.3$$

$$k_m = (2\pi v)^2 g / u^2 = \text{position of spectrum maximum}$$

$$\alpha = 0.0325 v^{2/3}$$

$$h^2 \simeq (u^4 / g^2) (5.2 \times 10^{-6} v^{-10/3}) = \text{mean-square wave height}$$

$$u = \text{wind speed (m sec}^{-1}\text{)}$$

$$g = 9.806 \text{ m sec}^{-2} = \text{gravitational constant}$$

This factor peaks at wavenumber k_m , and has the same equilibrium-range k^{-4} dependence as the Phillips and Pierson–Moskowitz models (corresponding to an f^{-5} frequency dependence). The JONSWAP spectrum has a sharper peak than previous models, as represented by the second term in the exponential argument. By setting that second term to zero and letting $\alpha = 0.0081$, one recovers the Pierson–Moskowitz (1964) model for fully developed seas that has been accepted over the previous decade.

The directional factor is given by

$$g(k, \theta) = [1/A(s)] |\cos[(\theta - \theta_w)/2]|^s \quad (\text{A5})$$

where

$$A(s) = \int_{-\pi}^{\pi} \cos^s(\theta/2) d\theta$$

$$s = 20(k/k_m)^\mu \quad \text{for } k > 1.1k_m$$

and

$$\mu = -2.33 - 1.45(2\pi v - 1.17)$$

while

$$s = 14 \left(\frac{k}{k_m} \right)^2 \quad \text{for } k < 1.1k_m$$

REFERENCES

- Barrick, D. E. (1968). Rough surface scattering based on the specular point theory, *IEEE Trans. Antennas Propag.* **AP-16**, 449–454.
- Barrick, D. E. (1972a). Remote sensing of sea state by radar. In “Remote Sensing of the Troposphere” (V. E. Derr, ed.), Ch. 12. U. S. Govt. Printing Office, Washington, D.C.
- Barrick, D. E. (1972b). Determination of mean surface position and sea state from the radar return of a short-pulse satellite altimeter. In “Sea Surface Topography from Space” (J. R. Apel, ed.), Vol. I, Ch. 16. U.S. Govt. Printing Office, Washington, D.C.
- Barrick, D. E., and Weber, B. L. (1977). On the nonlinear theory for gravity waves on the ocean’s surface. Part II: Interpretation and applications. *J. Phys. Oceanogr.* **7**, 11–21.
- Brandt, S. (1976). “Statistical and Computational Methods in Data Analysis.” North-Holland, Publ., Amsterdam.
- Brown, G. S. (1977). The average impulse response of a rough surface and its applications. *IEEE Trans. Antennas Propag.* **AP-25**, 67–74.
- Brown, G. S. (1979). Estimation of surface wind speeds using satellite-borne radar measurements at normal incidence. *J. Geophys. Res.* **84**(B8), 3974–3978.
- Choy, L. W., Hammond, D. L., and Uliana, E. A. (1984). Electromagnetic bias of 10 GHz radar altimetric measurements of MSL. *J. Mar. Geod.* **8**, 296–312.
- Ewing, G. C., ed. (1965). *Oceanography from space*. Woods Hole Oceanographic Institute, Ref. No. 65–10.

- Fedor, L. S., and Barrick, D. E. (1978). Measurement of ocean wave heights with a satellite radar altimeter, *EOS* **59**, 843–847.
- Fedor, L. S., and Brown, G. S. (1982). Waveheight and windspeed measurements from the SEASAT radar altimeter. *J. Geophys. Res.* **87**(C5), 3254–3260.
- Goldhirsh, J., and Walsh, E. J. (1982). Rain measurements from space using a modified SEASAT type radar altimeter. *IEEE Trans. Antennas Propag.* **AP-30**, 726–733.
- Hasselmann, K., Barnett, T. P., Bouws, E., Carlson, H., Cartwright, D. E., Enke, K., Ewing, J. A., Gienapp, H., Hasselmann, D. E., Kruseman, P., Meerburg, A., Müller, P., Olbers, D. J., Richter, K., Sell, W. and Walden, W. (1973). Measurements of wind-wave growth and swell decay during the Joint North Sea Wave Project. Deutsches Hydrographisches Institut, Hamburg.
- Hasselmann, K., Ross, D. B., Müller, P., and Sell, W. (1976). A parametric wave prediction model. *J. Phys. Oceanogr.* **6**, 200–228.
- Hasselmann, D. E., Duncel, M., and Ewing, J. A. (1980). Directional wave spectra observed during JONSWAP 1973. *J. Phys. Oceanogr.* **10**, 1264–1280.
- Hayne, G. S. (1981). Radar altimeter waveform modeled parameter recovery. NASA Tech. Memo. No. 73294. NASA Wallops Flight Center.
- Hayne, G. S., and Hancock, D. W., III (1982). Sea-state-related altitude errors in the SEASAT radar altimeter. *J. Geophys. Res.* **87**(C5), 3227–3231.
- Jackson, F. C. (1979). The reflection of impulses from a nonlinear random sea. *J. Geophys. Res.* **84**, 4939–4943.
- Kaula, W. M. (1970). “The Terrestrial Environment: Solid-Earth and Ocean Physics” (NASA Contractor Rep. No. 1579). MIT Press, Cambridge, Massachusetts.
- Lipa, B. J., and Barrick, D. E. (1981). Ocean surface height-slope probability density function from SEASAT altimeter echo. *J. Geophys. Res.* **86**(C11), 10921–10930.
- Longuet-Higgins, M. S. (1963). The effect of non-linearities on statistical distributions in the theory of sea waves. *J. Fluid Mech.* **17**, 459–480.
- MacArthur, J. L. (1978). SEASAT, a radar altimeter design description. *Johns Hopkins Univ. Appl. Phys. Lab. Rep.* SDO-5232.
- Pierson, W. J., and Moskowitz, L. (1964). A proposed spectral form for fully developed wind seas based on the similarity theory S.A. Kitaigorodsky. *J. Geophys. Res.* **69**(24).
- Townsend, W. F. (1980). An initial assessment of the performance achieved by the SEASAT-1 radar altimeter, *IEEE J. Oceanic Eng.* **OE-5**, 80–92.
- Walsh, E. J. (1979). Extraction of ocean waveheight and dominant wavelength from GEOS-3 data. *J. Geophys. Res.* **84**, 4003–4010.
- Walsh, E. J. (1981). Altimeter rain detection. NASA Tech. Memo 73291, NASA Wallops Flight Center.
- Walsh, E. J. Hancock, D. W., III, Hines, D. W., and Kenney, E. J. (1984). Electromagnetic bias of 36 GHz radar altimetric measurements of MSL. *J. Mar. Geod.* **8**, 265–296.
- Weber, B. L., and Barrick, D. E. (1977). On the nonlinear theory for gravity waves on the ocean’s surface. Part I: Derivations. *J. Phys. Oceanogr.* **7**, 3–10.
- Yaplee, B. S., Shapiro, S., Hammond, D. L., Au, B. D., and Uliana, E. A. (1971). Nanosecond radar observations of the ocean surface from a stable platform. *IEEE Trans. Geosci. Electron.* **GE-9**, 170–174.